Astronomy & Astrophysics manuscript no. output
March 18, 2025

Euclid Quick Data Release (Q1)

Optical and near-infrared identification and classification of point-like X-ray selected sources

Euclid Collaboration: W. Roster[⋆1], M. Salvato[1], J. Buchner[1], R. Shirley[1], E. Lusso[2,3], H. Landt[4], G. Zamorani[5], M. Siudek[6,7], B. Laloux[8,1], T. Matamoro Zatarain[9], F. Ricci[10,11], S. Fotopoulou[9], A. Ferré-Mateu[12,13], X. Lopez Lopez[14,5], N. Aghanim[15], B. Altieri[16], A. Amara[17], S. Andreon[18], N. Auricchio[5], H. Aussel[19], C. Baccigalupi[20,21,22,23], M. Baldi[24,5,25], A. Balestra[26], S. Bardelli[5], P. Battaglia[5], A. Biviano[21,20], A. Bonchi[27], E. Branchini[28,29,18], M. Brescia[30,8], J. Brinchmann[31,32], S. Camera[33,34,35], G. Cañas-Herrera[36,37,38], V. Capobianco[35], C. Carbone[39], J. Carretero[40,41], S. Casas[42], M. Castellano[11], G. Castignani[5], S. Cavuoti[8,43], K. C. Chambers[44], A. Cimatti[45], C. Colodro-Conde[12], G. Congedo[46], C. J. Conselice[47], L. Conversi[48,16], Y. Copin[49], F. Courbin[50,51], H. M. Courtois[52], M. Cropper[53], A. Da Silva[54,55], H. Degaudenzi[56], G. De Lucia[21], A. M. Di Giorgio[57], C. Dolding[53], H. Dole[15], F. Dubath[56], C. A. J. Duncan[47], X. Dupac[16], S. Dusini[58], S. Escoffier[59], M. Fabricius[1,60], M. Farina[57], R. Farinelli[5], F. Faustini[27,11], S. Ferriol[49], F. Finelli[5,61], P. Fosalba[62,7], N. Fourmanoit[59], M. Frailis[21], E. Franceschi[5], S. Galeotta[21], K. George[60], B. Gillis[46], C. Giocoli[5,25], J. Gracia-Carpio[1], B. R. Granett[18], A. Grazian[26], F. Grupp[1,60], S. Gwyn[63], S. V. H. Haugan[64], W. Holmes[65], I. M. Hook[66], F. Hormuth[67], A. Hornstrup[68,69], P. Hudelot[70], K. Jahnke[71], M. Jhabvala[72], E. Keihänen[73], S. Kermiche[59], A. Kiessling[65], B. Kubik[49], M. Kümmel[60], M. Kunz[74], H. Kurki-Suonio[75,76], Q. Le Boulc'h[77], A. M. C. Le Brun[78], D. Le Mignant[79], S. Ligori[35], P. B. Lilje[64], V. Lindholm[75,76], I. Lloro[80], G. Mainetti[77], D. Maino[81,39,82], E. Maiorano[5], O. Mansutti[21], S. Marcin[83], O. Marggraf[84], M. Martinelli[11,85], N. Martinet[79], F. Marulli[14,5,25], R. Massey[86], D. C. Masters[87], E. Medinaceli[5], S. Mei[88,89], M. Melchior[90], Y. Mellier[91,70], M. Meneghetti[5,25], E. Merlin[11], G. Meylan[92], A. Mora[93], M. Moresco[14,5], L. Moscardini[14,5,25], R. Nakajima[84], C. Neissner[94,41], S.-M. Niemi[36], J. W. Nightingale[95], C. Padilla[94], S. Paltani[56], F. Pasian[21], K. Pedersen[96], W. J. Percival[97,98,99], V. Pettorino[36], S. Pires[19], G. Polenta[27], M. Poncet[100], L. A. Popa[101], L. Pozzetti[5], F. Raison[1], R. Rebolo[12,102,13], A. Renzi[103,58], J. Rhodes[65], G. Riccio[8], E. Romelli[21], M. Roncarelli[5], R. Saglia[60,1], Z. Sakr[104,105,106], A. G. Sánchez[1], D. Sapone[107], B. Sartoris[60,21], J. A. Schewtschenko[46], M. Schirmer[71], P. Schneider[84], T. Schrabback[108], A. Secroun[59], G. Seidel[71], M. Seiffert[65], S. Serrano[62,109,7], P. Simon[84], C. Sirignano[103,58], G. Sirri[25], L. Stanco[58], J. Steinwagner[1], P. Tallada-Crespí[40,41], D. Tavagnacco[21], A. N. Taylor[46], I. Tereno[54,110], S. Toft[111,112], R. Toledo-Moreo[113], F. Torradeflot[41,40], I. Tutusaus[105], L. Valenziano[5,61], J. Valiviita[75,76], T. Vassallo[60,21], G. Verdoes Kleijn[114], A. Veropalumbo[18,29,28], Y. Wang[87], J. Weller[60,1], A. Zacchei[21,20], F. M. Zerbi[18], I. A. Zinchenko[60], E. Zucca[5], V. Allevato[8], M. Ballardini[115,116,5], M. Bolzonella[5], E. Bozzo[56], C. Burigana[117,61], R. Cabanac[105], A. Cappi[5,118], D. Di Ferdinando[25], J. A. Escartin Vigo[1], L. Gabarra[119], M. Huertas-Company[12,6,120,121], J. Martín-Fleitas[93], S. Matthew[46], N. Mauri[45,25], R. B. Metcalf[14,5], A. Pezzotta[122,1], M. Pöntinen[75], C. Porciani[84], I. Risso[123], V. Scottez[91,124], M. Sereno[5,25], M. Tenti[25], M. Viel[20,21,23,22,125], M. Wiesmann[64], Y. Akrami[126,127], I. T. Andika[128,129], S. Anselmi[58,103,130], M. Archidiacono[81,82], F. Atrio-Barandela[131], C. Benoist[118], K. Benson[53], D. Bertacca[103,26,58], M. Bethermin[132], L. Bisigello[26], A. Blanchard[105], L. Blot[133,130], H. Böhringer[1,134,135], M. L. Brown[47], S. Bruton[136], A. Calabro[11], F. Caro[11], C. S. Carvalho[110], T. Castro[21,22,20,125], F. Cogato[14,5], A. R. Cooray[137], O. Cucciati[5], S. Davini[29], F. De Paolis[138,139,140], G. Desprez[114], A. Díaz-Sánchez[141], J. J. Diaz[6,12], S. Di Domizio[28,29], J. M. Diego[142], A. Enia[24,5], Y. Fang[60], A. G. Ferrari[25], A. Finoguenov[75], A. Fontana[11], A. Franco[139,138,140], K. Ganga[88], J. García-Bellido[126], T. Gasparetto[21], V. Gautard[143], E. Gaztanaga[7,62,144], F. Giacomini[25], F. Gianotti[5], G. Gozaliasl[145,75], M. Guidi[24,5], C. M. Gutierrez[146], A. Hall[46], W. G. Hartley[56], S. Hemmati[147], C. Hernández-Monteagudo[13,12], H. Hildebrandt[148], J. Hjorth[96], J. J. E. Kajava[149,150], Y. Kang[56], V. Kansal[151,152], D. Karagiannis[115,153], K. Kiiveri[73], C. C. Kirkpatrick[73], S. Kruk[16], J. Le Graet[59], L. Legrand[154,155], M. Lembo[115,116], F. Lepori[156], G. Leroy[4,86], G. F. Lesci[14,5], J. Lesgourgues[42], L. Leuzzi[14,5], T. I. Liaudat[157], A. Loureiro[158,159], J. Macias-Perez[160], G. Maggio[21], M. Magliocchetti[57], F. Mannucci[2], R. Maoli[161,11], C. J. A. P. Martins[162,31], L. Maurin[15], M. Miluzio[16,163], P. Monaco[164,21,22,20], C. Moretti[23,125,21,20,22], G. Morgante[5], K. Naidoo[144], A. Navarro-Alsina[84], S. Nesseris[126], F. Passalacqua[103,58], K. Paterson[71], L. Patrizii[25], A. Pisani[59,165], D. Potter[156], S. Quai[14,5], M. Radovich[26], S. Sacquegna[138,139,140], M. Sahlén[166], D. B. Sanders[44], E. Sarpa[23,125,22], A. Schneider[156],

D. Sciotti[11,85], E. Sellentin[167,38], F. Shankar[168], L. C. Smith[169], K. Tanidis[119], G. Testera[29], R. Teyssier[165], S. Tosi[28,123], A. Troja[103,58], M. Tucci[56], C. Valieri[25], A. Venhola[170], D. Vergani[5], G. Verza[171], P. Vielzeuf[59], A. Viitanen[73,11], N. A. Walton[169], E. Soubrie[15], and D. Scott[172]

(Affiliations can be found after the references)

Received ; accepted

ABSTRACT

To better understand the role of active galactic nuclei (AGN) in galaxy evolution, it is crucial to achieve a complete and pure AGN census. X-ray surveys are key to this, but identifying their counterparts (CTPs) at other wavelengths remains challenging due to their larger positional uncertainties and limited availability of deeper, uniform ancillary data. *Euclid* is revolutionising this effort, offering extensive coverage of nearly the entire extragalactic sky, particularly in the near-infrared bands, where AGN are more easily detected. With the first Euclid Quick Data Release (Q1), we tested and validated methods for identifying, classifying, and determining the redshifts of *Euclid* CTPs to known point-like sources from major X-ray surveys, including XMM-*Newton*, *Chandra*, and eROSITA. Using Bayesian statistics, combined with machine learning (ML), as incorporated in the algorithm `NWAY`, we identify the CTPs to 11 286 X-ray sources from the three X-ray telescopes. For the large majority of 10 194 sources, the association is unique, with the remaining $\sim 10\%$ of multi-CTP cases equally split between XMM-*Newton* and eROSITA. Six percent of the *Euclid* CTPs are detected in more than one X-ray survey. ML is then used to distinguish between Galactic (8%) and extragalactic (92%) sources. We computed photo-zs using deep learning for the 8617 sources detected in the 10th data release of the DESI Legacy Survey, reaching an accuracy and a fraction of outliers of about 5%. Based on their X-ray luminosities, over 99% of CTPs identified as extragalactic are classified as AGN, most of which appear unobscured according to their hardness ratios. With this paper, we release our catalogue, which includes identifiers, basic X-ray properties, the reliability of the associations, and additional property extensions such as Galactic/extragalactic classifications and photometric/spectroscopic redshifts. We also provide probabilities for sub-selecting the sample based on purity and completeness, allowing users to tailor the sample according to their specific needs.

Key words. Methods: statistical, data analysis; Surveys; Catalogues; Galaxies: active; X-rays: galaxies

1. Introduction

Active galactic nuclei (AGN[1]), which rank among the most energetic phenomena in the Universe, play a pivotal role in shaping the evolutionary trajectories of galaxies throughout cosmic time. Their activity is fundamentally driven by the accretion of matter onto supermassive black holes (SMBHs) from their surrounding environment (e.g., Salpeter 1964; Lynden-Bell 1969; Pringle & Rees 1972; Shakura & Sunyaev 1973; Lynden-Bell & Pringle 1974; Kormendy & Ho 2013). Situated at the centres of galaxies, AGN emit intense radiation across the entire electromagnetic spectrum, ranging from radio waves to γ-rays (e.g., Elvis et al. 1994; Urry & Padovani 1995; Padovani et al. 2017). While this is particularly true for quasi-stellar objects (QSOs), it is important to note that the range of activity, emission, and interaction of AGN spans a broad spectrum, with different AGN exhibiting varying levels of energy outputs (e.g., Peterson 1997; Pierce et al. 2010; Pović et al. 2012; Bettoni et al. 2015).

Consequently, with enough coupling efficiency, this allows AGN to exert significant influence over both their host galaxies and the growth of their central SMBHs, where the interplay between AGN activity and the respective host is believed to regulate star formation and shape the morphology of galaxies. Here, energetic feedback drives powerful winds and outflows, impacting the surrounding interstellar and intergalactic medium (Greene et al. 2011; Cielo et al. 2018). These close connections are supported by fundamental scaling relations that link the SMBH mass to various galactic properties. Notable among these are the $M_{\rm BH} - \sigma$ relation, which ties BH mass to the velocity dispersion of stars in the galaxy's bulge (Gebhardt et al. 2000; Ferrarese & Merritt 2000), and the $M_{\rm BH} - M_*$ relation, which connects it to the stellar mass of the host galaxy (Magorrian et al. 1998; Häring & Rix 2004; Gültekin et al. 2009; Sani et al. 2011; Shankar et al. 2016; Suh et al. 2020), pointing to an intricate co-evolution of the systems (Kormendy & Ho 2013; Heckman & Best 2014; Madau & Dickinson 2014; Euclid Collaboration: Bisigello et al. 2024). However, the physical mechanisms driving this connection remain under debate, highlighting the need to construct a complete picture of AGN diversity and complexity to better understand galaxy formation and transformation across the history of the Universe (e.g., Aird et al. 2010; Buchner et al. 2015; Georgakakis et al. 2015; Ananna et al. 2017; Morganti 2017; Delvecchio et al. 2017; Husemann & Harrison 2018; Harrison & Ramos Almeida 2024).

Despite significant advancements over the years, the current AGN census remains incomplete due to inherent biases introduced to individual samples by various multi-wavelength selection methods, each favouring specific properties of the population (Messias et al. 2014; Padovani et al. 2017; Delvecchio et al. 2017; Lyu et al. 2022; Green et al. 2024). Comprehensive wavelength coverage is essential for identifying diverse AGN types across all redshifts, with each method capitalising on the dominant physical processes within its waveband to uncover unique facets of AGN activity, where the AGN dominates the spectral energy distribution (SED) of its host galaxy (Padovani et al. 2017). For instance, radio observations are effective in identifying jet-dominated AGN (De Breuck et al. 2002; Smolčić et al. 2017), while optical diagnostics (Feltre et al. 2016), such as emission line ratios (e.g., BPT diagrams as in Baldwin et al. 1981; Veilleux & Osterbrock 1987; Juneau et al. 2014), are widely used to distinguish AGN from star-forming galaxies by probing ionisation mechanisms. Other selections include colour or variability (e.g., Richards et al. 2002; Bongiorno et al. 2010; Bovy et al. 2012; Donley et al. 2012; Kirkpatrick et al. 2013; Peters et al. 2015; Palanque-Delabrouille et al. 2016; Lusso & Risaliti 2016). Soft X-ray selection excels at detecting unobscured accretion-powered emission (e.g., Hasinger 2008; Brandt & Hasinger 2005; Nandra et al. 2015) and can be complemented by mid-infrared (MIR) observations (e.g., Stern et al. 2012; Assef et al. 2013), which penetrate dense dust clouds effectively (Hickox & Alexander 2018). Notably, the significantly higher contrast between the intrinsic brightness of accreting SMBHs

* e-mail: wroster@mpe.mpg.de

[1] Used interchangeably in both singular and plural cases

and their host galaxies in X-rays, as opposed to other wavelengths, makes this selection one of the most uncontaminated, providing pure AGN samples of larger diversity (Xue et al. 2011a; Donley et al. 2012). To combine different observational perspectives of AGN, these X-ray samples must then be paired with ancillary multi-wavelength data.

In the past, identifying multi-wavelength counterparts (CTPs) for X-ray selected sources was a significant hurdle in AGN characterisation and redshift estimation (Salvato et al. 2018). While combining data from multiple wavelengths is crucial for constructing a more complete picture of AGN, the process of cross-identifying sources remains complicated. Due to the significant positional uncertainties in X-ray surveys, confidently linking most X-ray sources to a single, definitive CTP in e.g., optical, infrared, or radio surveys is challenging, except for the brightest cases. These uncertainties, along with the uneven spatial coverage of ancillary data, further complicate the task of reliably pinpointing AGN across different surveys. Consequently, a simple coordinate match is insufficient, and more sophisticated methods are needed for accurate cross-identification. For this purpose, machine learning (ML) algorithms that integrate multi-wavelength source classification approaches have become increasingly prevalent (e.g., Cavuoti et al. 2014; Brescia et al. 2015; Karsten et al. 2023; Cooper et al. 2023; Daoutis et al. 2023; Zeraatgari et al. 2024; Pérez-Díaz et al. 2024; Mechbal et al. 2024).

While challenging to this date, the European Space Agency's *Euclid* satellite will help overcome this limitation due to its uniform depth and wide coverage (Laureijs et al. 2011; Euclid Collaboration: Mellier et al. 2024). At the same time, *Euclid*'s depth results in very high source densities, increasing the risk of unforced misidentification and chance alignments. Over its six-year mission lifetime, *Euclid* will cover a total of $\sim 14\,000\,\mathrm{deg}^2$ in the Euclid Wide Survey (EWS, Euclid Collaboration: Scaramella et al. 2022), expected to detect billions of sources. In addition to its cosmological objectives, *Euclid* will play a crucial role in the detection and characterization of AGN, expecting to detect at least 10 million of them (Euclid Collaboration: Bisigello et al. 2024; Euclid Collaboration: Lusso et al. 2024; Euclid Collaboration: Selwood et al. 2025). To achieve these goals, *Euclid* employs two main instruments: the VISible imager (VIS, Euclid Collaboration: Desprez et al. 2020; Euclid Collaboration: Cropper et al. 2024), covering wavelengths from 0.53 to 0.90 µm (I_E) and the Near-Infrared Spectrometer and Photometer (NISP, Maciaszek et al. 2022; Euclid Collaboration: Jahnke et al. 2024) operating in the near-infrared, with photometric measurements in three bands (Y_E, J_E, and H_E), covering in total the wavelength range from 0.95 to 2.02 µm, while also including a slitless spectrograph for the detection of emission lines.

With the first Euclid Quick Data Release (Q1) we can now begin building and testing the necessary machinery for identifying and characterising AGN previously selected in the X-rays, where we aim to leverage *Euclid*'s depth, resolution and wavelength coverage to provide more secure associations. This initial testing will form the foundation for refining our methods and ensuring accurate AGN identification as more data becomes available over the next years.

In this paper, we address the task of reliably associating X-ray sources with their *Euclid* CTPs and investigate their respective NIR properties as a function of X-ray flux, among other properties. The paper is structured as follows: Sect. 2 gives an overview of the Q1 data. Section 3 introduces the X-ray source catalogues used in this work, while Sect. 4 outlines the approach to identifying CTPs. Section 5 describes how using a sample of sources clearly characterised with the 10th Data Release of the Legacy Survey (Dey et al. 2019), we assign a Galactic/extragalactic nature to our sources using *Euclid* photometry. In Sect. 6, we compute photometric redshifts for all CTPs. Section 7 displays CTP sample properties and Sect. 8 explains the release of the catalogues and how to use them. A summary and discussion are given in the final Sect. 9.

In this paper, unless stated otherwise, we express magnitudes in the AB system (Oke & Gunn 1983) and adopt a flat ΛCDM cosmology with $H_0 = 70\,\mathrm{km\,s^{-1}\,Mpc^{-1}}$, $\Omega_\mathrm{m} = 0.3$ and $\Omega_\Lambda = 0.7$, to facilitate direct comparison with similar works from literature.

2. Euclid Q1 fields

Euclid Q1 marks the initial data release with a footprint area of $\sim 63.1\,\mathrm{deg}^2$ (Euclid Collaboration: Mellier et al. 2024). It consists of observations making up the Euclid Deep Survey (EDS), selected for their considerable multi-wavelength coverage. However, the data is currently at the depth of the EWS, with a 5σ depth of $I_\mathrm{E}\,(\mathrm{AB}) = 24.5$ for point sources. The EDS targets three important Euclid Deep Fields (EDFs, see Fig. 1): the EDF Fornax (EDF-F), EDF South (EDF-S), and the EDF North (EDF-N). For more details, we refer the reader to Euclid Collaboration: Aussel et al. (2025).

The catalogues provide comprehensive photometric information across all four *Euclid* bands (Euclid Collaboration: McCracken et al. 2025; Euclid Collaboration: Polenta et al. 2025; Euclid Collaboration: Romelli et al. 2025). In addition to the *Euclid* bands, the catalogue is supplemented with ground-based photometry in the *ugriz* optical bands, where available, sourced from various instruments depending on their access to the northern or southern extragalactic sky. Photometric measurements are provided as both template/Sérsic model fits and fluxes extracted within apertures corresponding to radii of 1 – 4 times the seeing full-width at half maximum (FWHM).

3. The X-ray surveys

X-ray surveys are often constrained by the flux detection limit of the most sensitive X-ray telescopes, which typically operate with small fields of view. Therefore, surveys with different observational strategies need to be combined to facilitate the characterisation of the full AGN population. Pencil-beam surveys that provide exceptionally deep observations, valuable for probing faint AGN and for characterising the low-luminosity end of the AGN population, are limited in sky coverage and, consequently, miss rare (bright or distant) sources (e.g., Brusa et al. 2010; Hsu et al. 2014; Nandra et al. 2015; Marchesi et al. 2016; Luo et al. 2017; Oh et al. 2018). Subsequently, the data releases of XMM-*Newton* 4XMM DR14 (Webb et al. 2020) and *Chandra* Source Catalogue 2 (CSC 2.0, Evans et al. 2024) feature outstanding sensitivity for X-ray selected sources but cover relatively small regions of the sky.

On the other hand, wide-area surveys are crucial for complementing pointed observations and uncover those AGN missed (e.g., Ananna et al. 2017; Fotopoulou et al. 2016). Therefore, we incorporate data from the extended *Roentgen* Survey with an Imaging Array (eROSITA; Predehl et al. 2021) DR1 Main sample (Merloni et al. 2024). As part of the ongoing eROSITA All-Sky Survey (eRASS), these data provide homogeneous, soft X-ray coverage of the entire extragalactic sky. While eROSITA's positional accuracy is somewhat pourer than that of XMM-

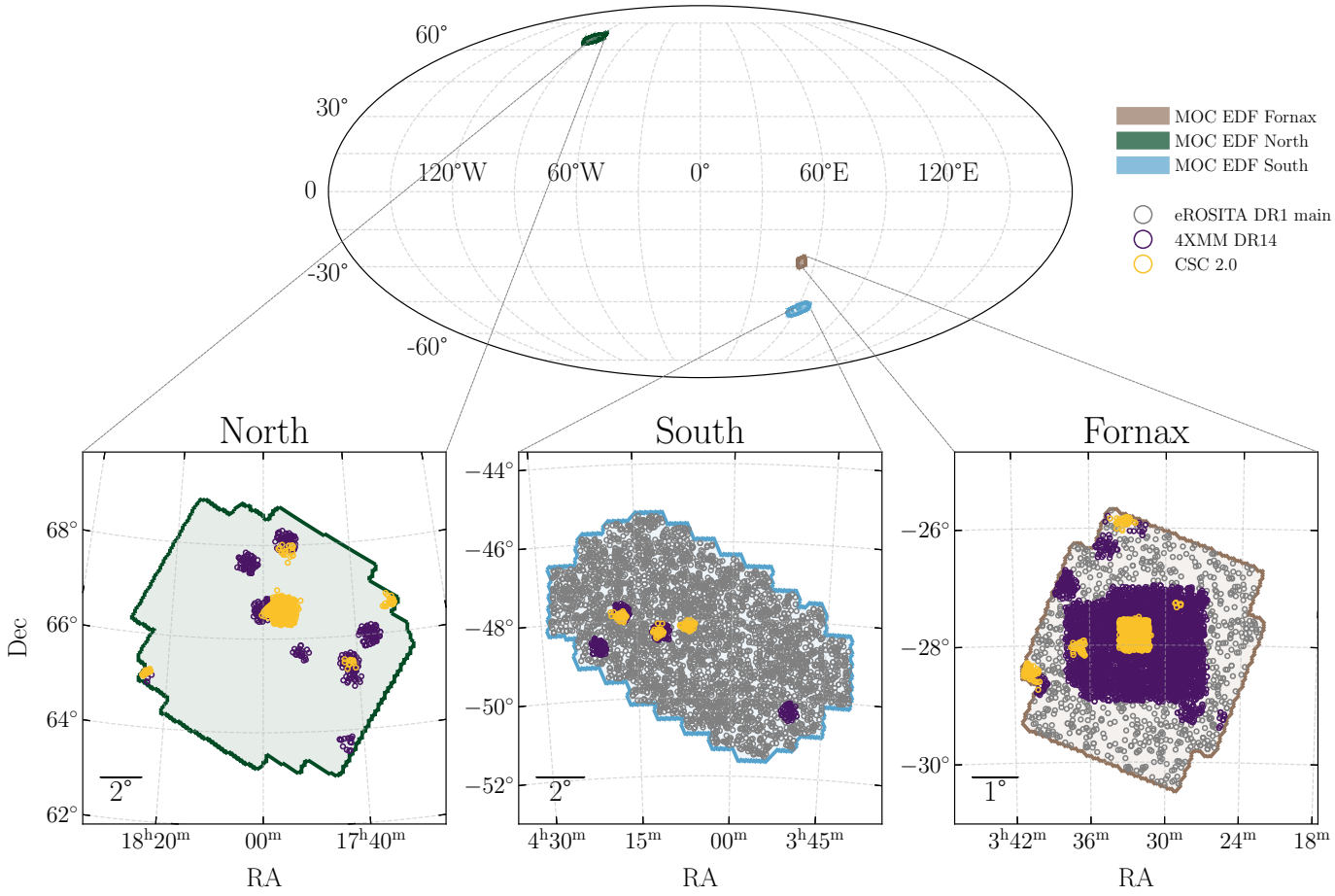

Fig. 1. Sky coverage of the EDF fields and corresponding X-ray source distributions. *Top:* Mollweide projection of the sky, indicating the locations of EDF-N, EDF-S, and EDF-F using their Multi-Order Coverage maps (MOCs). *Bottom:* zoomed-in views of each EDF, overlaid with X-ray sources from the eROSITA-DE DR1 catalogue (grey), the XMM-*Newton* 4XMM DR14 catalog (purple), and the *Chandra* Source Catalog 2.0 (orange), illustrating the overlap between *Euclid*'s deep fields and existing X-ray source catalogues.

Newton and *Chandra*, its unparalleled breadth allows us to include a significantly larger sample of sources, enhancing the statistical power of our analysis and ensuring a more comprehensive AGN census (see Fig. 1 and Table 1). In the following subsections, we describe the selection criteria applied to the catalogues from each X-ray survey.

3.1. XMM-Newton

The XMM-*Newton* space-telescope provides some of the deepest and most detailed X-ray imaging available, with a spatial resolution of approximately 6″ and positional uncertainties typically below 1 – 2″. The data used in this study include both targeted and serendipitous observations, selected from the 4XMM-DR14 catalogue[2], which offers multi-band flux measurements and quality flags. To prepare the sample, point-like sources were filtered based on their extent likelihood and positional uncertainties: `SC_EXT_ML` < 10, `SC_EXTENT` < 10 and `SC_POSERR` < 10″, where the threshold for the positional uncertainty is motivated by the respective distribution as a function of flux as shown in Fig. 2. This effectively reduces the computational load for cross-matching with *Euclid*. To be consistent with other X-ray surveys, we compute the X-ray flux F_x for the 0.5 – 2 keV band as

$$\mathrm{F_X} = \mathrm{SC\_EP\_2\_FLUX_{0.5-1.0keV}} + \mathrm{SC\_EP\_3\_FLUX_{1.0-2.0keV}}\,, \tag{1}$$

and its uncertainty as

$$\mathrm{EF_X} = \sqrt{\mathrm{SC\_EP\_2\_FLUX\_ERR^2} + \mathrm{SC\_EP\_3\_FLUX\_ERR^2}}\,, \tag{2}$$

by combining the 0.5 – 1 keV, and 1 – 2 keV band fluxes and errors.

3.2. Chandra

The *Chandra* X-ray space-telescope provides sub-arcsecond angular resolution, which allows precise localisation of sources and makes it particularly effective in crowded or complex fields. Our sample incorporates sources from the CSC 2.0 catalogue[3]. To subsample only point-like sources, we select sources with the extended flag, f_e, set to zero. The 0.5 – 2 keV X-ray flux and its uncertainty are computed as

[2] catalogue and data model description available at https://cdsarc.cds.unistra.fr/viz-bin/cat/IX/69

[3] https://vizier.cds.unistra.fr/viz-bin/VizieR?-source=IX/57&-to=3

Table 1. Sample sizes for the three X-ray catalogues at various stages.

X-ray catalogue (1)	Number of sources (2)	AND point-like (3)	AND POSERR < limit (4)	EDF-F (5)	EDF-N (6)	EDF-S (7)
4XMM DR14	692 109	612 521	612 504	4523	445	273
CSC 2.0	317 167	296 473	296 162	1016	506	147
eROSITA DR1 main	898 812	879 153	878 984	1012	0	3369

Notes. (1) X-ray catalogue, (2) total number of X-ray sources (starting from unique source ID entries and QFs set to zero), (3) after applying the point-like source criterion, and (4) after following the application of the positional error threshold. Columns (5), (6), and (7) give the respective number of sources in each EDF.

$$F_X = \mathrm{Flux}_{0.5-1.2\,\mathrm{keV}} + \mathrm{Flux}_{1.2-2.0\,\mathrm{keV}}\,, \quad (3)$$

$$EF_X = \sqrt{(\mathrm{B\_Fluxs} - \mathrm{b\_Fluxs})^2 + (\mathrm{B\_Fluxm} - \mathrm{b\_Fluxm})^2}\,, \quad (4)$$

with $\mathrm{Flux}_{0.5-1.2\,\mathrm{keV}}$ and $\mathrm{Flux}_{1.2-2.0\,\mathrm{keV}}$ referring to the default CSC 2.0 soft and medium bands, respectively, while (B) and (b) represent the upper and lower 1 σ error margins. The positional uncertainties are determined using the 2 σ errors along the semi-major (r_0) and semi-minor (r_1) axes of the error ellipse provided in the source catalogue, as

$$\mathrm{C\_POSERR} = \sqrt{\frac{(r_0/2)^2 + (r_1/2)^2}{2}}\,, \quad (5)$$

and downsample the CSC 2.0 catalogue such that C_POSERR < 10″, to be consistent with 4XMM DR14 (see Fig. 2).

3.3. eROSITA

The eROSITA-DE DR1 main catalogue[4] offers comprehensive coverage of the western galactic hemisphere. While it does not include the EDF-N region (see Fig. 1), with a half energy width (HEW) of 26″ and a soft X-ray energy range of 0.2 – 2.3 keV, eROSITA offers a uniform data set ideal for large statistical studies. The data preparation for eROSITA included filtering for reliable point-source detections with EXT_LIKE = 0. Additionally, we required that all nine quality flags (QFs) are set to zero, and applied a cut in positional uncertainty of POS_ERR < 20″(refer to Table 1).

The choice to permit larger positional uncertainties in the eROSITA DR1 sample, as opposed to the XMM-*Newton* and *Chandra* samples, is guided by the comparison of their error distributions shown in Fig. 2. This approach ensures the retention of the majority of the sample while excluding only a small number of outliers with exceptionally high positional errors. We intentionally avoid applying more restrictive criteria, such as minimum flux, signal-to-noise ratio (S/N), isolated environments, detection likelihoods, or other observational limitations, in order to prevent excluding sources that could potentially be identified by *Euclid*. An overview of the sample sizes is given in Table 1. By setting this threshold, we aim to optimise the balance between maintaining a robust sample and minimising the computational effort required for CTP identification within the defined error limits.

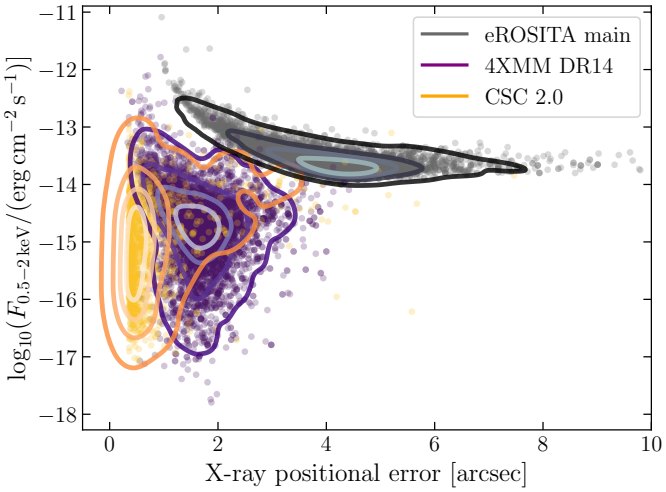

Fig. 2. X-ray fluxes in the 0.5 – 2 keV band plotted against positional uncertainties for sources from the 4XMM DR14, CSC 2.0, and eROSITA-DE/DR1 catalogues.

4. Identification of CTPs

Until recently, the identification of CTPs was primarily performed using maximum likelihood matching (e.g., Sutherland & Saunders 1992). This approach considers the separation between sources in the primary catalogue (e.g., X-ray) and the secondary multiwavelength catalogue, the positional uncertainties of the primary sources, and the magnitude distribution of sources in the ancillary catalogues within a certain radius from the primary sources. While this method has been applied successfully in cases with small positional errors and bright sources (see e.g., Naylor et al. 2013; Brusa et al. 2010; Xue et al. 2011b), its reliability decreases in situations where positional errors are large, and more than one photometric point is necessary for identifying the correct CTP or when multiple potential CTPs exist within the search radius. In such cases, positional matching often fails to provide a robust identification.

4.1. NWAY

To address these challenges, bayesian statistic needs to be invoked (Budavári & Szalay 2008). With this in mind, algorithms such as NWAY (Salvato et al. 2018), and XMATCH (Pineau et al. 2017) were developed. Unlike the others, NWAY also allows for the adoption of priors in addition to positional matches between multiple catalogues. It refines its matching procedure by being able to supplement one or more features, such as colours, mag-

[4] https://erosita.mpe.mpg.de/dr1/AllSkySurveyData_dr1/Catalogues_dr1/

Table 2. Overview of *Euclid* features used to train the random forest classifier for the photometric prior used in `NWAY`.

Feature	Description
dered_*_flux	deredened template flux in I_E, Y_E, J_E, and H_E
colour_*	deredened template colour for $I_E - Y_E$, $I_E - J_E$, $I_E - H_E$, $Y_E - J_E$, $Y_E - H_E$, and $J_E - H_E$
snr_*	S/N for template I_E, Y_E, J_E, and H_E
point_like_prob	probability between 0 and 1 that the source is point-like
vis_det	binary flag, where $\begin{cases}\text{source is detected in the VIS mosaic (1)}, \\ \text{source is only detected in the NIR mosaic (0)}\end{cases}$

Notes. Deredened fluxes are calculated by correcting for Milky Way (MW) extinction, following the procedure for obtaining intrinsic magnitudes described by Cuillandre et al. (2024).

nitudes, and S/N, into likelihood ratios used for CTP identification. These priors, based on (anti-) correlations between source properties of the target and field populations, allow `NWAY` to improve the likelihood of finding true matches, boosting the accuracy significantly over methods that rely solely on positional information.

4.1.1. The integration of priors in `NWAY`

Colour and magnitude priors are posteriors that encode knowledge from data or probabilistic distributions that describe the expected properties of true CTPs for the sources in the primary catalogue. For example, an AGN selected in X-rays is likely to have distinct colours (e.g., redder MIR colours due to dust) and magnitudes compared to stars or inactive galaxies. The difference between the methods resides then in the adoption of specific features able to distinguish an X-ray emitter (regardless of its Galactic or extragalactic nature) from a random source in the field (Salvato et al. 2022). `NWAY` uses these priors to add additional dimensions to calculate a more nuanced likelihood ratio. This reduces ambiguity, especially in crowded fields or cases with large positional uncertainties.

For instance, in the ROSAT All-Sky Survey (2RXS, Boller et al. 2016), Salvato et al. (2018) improved CTP identification by incorporating a 2D prior based on the W2 magnitude and W1−W2 colour from AllWISE (Wright et al. 2010), effectively separating out AGN. In the more recent application to the eROSITA Final Equatorial-Depth Survey (eFEDS, Brunner et al. 2022), Salvato et al. (2022) defined a prior that utilised not only magnitudes and colours from the Legacy Survey Data Release 10 (Dey et al. 2019), but also S/N in all bands (*griz*, W1, W2, W3, and W4), as well as properties, such as proper motion, from *Gaia* DR3 (Vallenari et al. 2023) when available. For further details on the formalism, we refer to the `NWAY` documentation[5].

4.1.2. Q1 prior

In this work, we have adopted the same principle as described in the previous subsection, but restricted ourselves to using only photometric features from *Euclid*. To build priors based on multiple features, `NWAY` can incorporate probabilities derived from ML models, such as a random forest (RF) classifier (the `sklearn` implementation, Pedregosa et al. 2011). We start by utilising a sample of secure CTPs to X-ray sources from 4XMM DR11 (Traulsen et al. 2020) and CSC 2.0 for training the RF as presented by Salvato et al. (2022). `NWAY` is then applied to identify CTPs for these X-ray sources in the EDF catalogues. A search radius of three times the positional error threshold is set around each X-ray source to include all potential EDF matches within this radius. This large search radius ensures that widely separated CTPs are not missed, even for sources with the largest positional uncertainties. The sky coverage of each X-ray sample per EDF is calculated to account for overlapping search windows. Specifically, while the coverage for the X-ray sample is given by its multi-order coverage map (MOC) or pointing, the EDF coverage is derived as

$$A_{\text{field}} = N_{\text{X-ray}} \cdot \pi \cdot (\text{POSERR})^2 - \text{A}_{\text{overlap}}\,, \tag{6}$$

where $N_{\text{X-ray}}$ corresponds to the number of X-ray sources and A_{overlap} is the overlapping area of adjacent search windows. Following the methodology outlined in Salvato et al. (2018), these coverage areas are used to compute the number densities, which inform two key probabilities: `p_any` (the probability that an X-ray source has a CTP) and `p_i` (the probability that each EDF source within the search radius is the correct CTP). `NWAY` identifies the most likely CTP for each X-ray source by selecting the EDF source with the highest `p_i` value. This CTP is considered the primary match. To assess the reliability of this identification, the `p_any` value is used as a confidence threshold. All sources identified as primary matches (`match_flag` == 1) with `p_any` > 0.85, form the target sample. In addition, for every X-ray source, all other EDF sources within the search radius that are not the primary match are collected into a field population, provided `p_any` < 0.1. This field population serves as a representation of non-X-ray sources, providing a comparison set for training the RF. To label the data sets, X-ray CTPs are assigned a target class of '1', while field objects are labelled as '0'. The *Euclid*-only training features utilised for the RF classifier are outlined in Table 2. At present, photometry and colours from different apertures are not included as features, as the aperture sizes vary between sources despite sharing the same designation.

Future data releases may standardise aperture sizes across all objects, also enhancing the RF classifier's ability to leverage the relationship between light profiles and X-ray emission. To evaluate model performance, 15% of the training data set (6000 field and 1730 target sources) is randomly set aside as a test set. The RF model is configured with 200 decision trees, with splits allowed if at least 25 samples remain in a branch. Per decision tree construction, 10 photometric features are considered and bootstrap sampling is applied to the training set for building the ensemble of trees. Since the data set is highly imbalanced, with field objects vastly outnumbering CTPs of X-ray sources, a weighting scheme is implemented to automatically adjust the contribution of each class during training (Salvato et al. 2022). This ensures the model effectively learns to differentiate between the two classes despite the imbalance. The classifier outputs a

[5] https://github.com/JohannesBuchner/NWAY

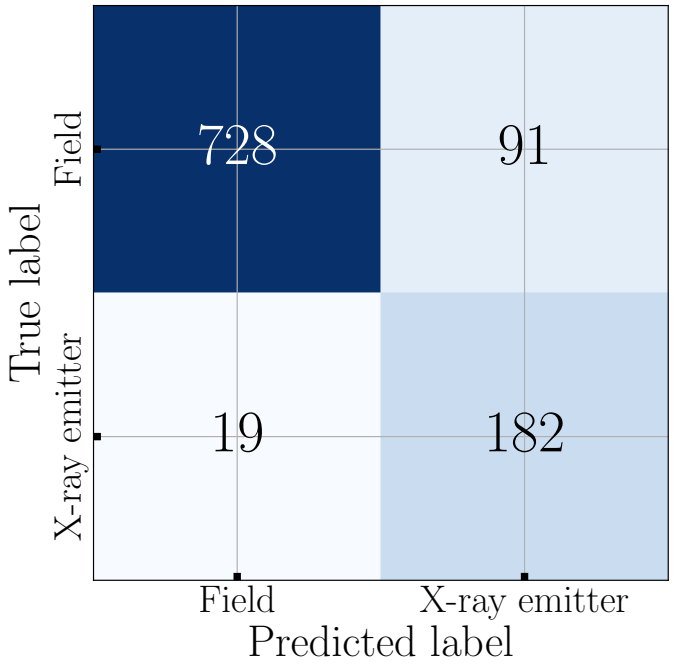

Fig. 3. Confusion matrix from the RF prediction on an independent test set. X-ray sources are labelled as 'X-ray emitter' while field objects as 'Field'. Numbers on the diagonal correspond to correctly predicted classes TP (bottom right) and TN (top left) while those off-diagonal refer to falsely predicted classes FP (top right) and FN (bottom left).

probability score X-ray, the predicted likelihood of a candidate CTP being X-ray emitting. $P_{\text{X-ray}}$ is used for class prediction, where `NWAY` retains candidates with $P_{\text{X-ray}} < 50\%$ if their astrometric configuration strongly supports a match. Importantly, the probability $P_{\text{X-ray}}$ is derived exclusively from photometric properties, independent of positional uncertainties, enabling it to be seamlessly integrated into `NWAY`'s Bayesian framework, complementing astrometric priors with photometric information.

We quantify the classification quality by comparing the input labels and predicted classes as: (i) true positive (TP, where label = 1 and prediction = 1); (ii) true negative (TN, where label = 0 and prediction = 0); (iii) false positive (FP, where label = 0 and prediction = 1); and (iv) false negative (FN, where label = 1 and prediction = 0). The model's performance is summarised in the confusion matrix shown in Fig. 3, assessed by acquiring these values for the test set (see e.g., Fotopoulou & Paltani 2018). We define the following measures of quality for the classifier:

- accuracy = (TP+TN)/(TP+TN+FP+FN) ;
- precision = TP/(TP+FP) ;
- recall = TP/(TP+FN) ;
- fall-out = FP/(TN+FP) .

The trained model achieves strong performance, with high accuracy of 89% and recall of 91%, indicating that most real X-ray emitters are correctly identified. The contamination rate remains low, with a fractional leakage of 11%. The fall-out fraction can, in principle, be reduced by including more field objects, though at the price of reduced recall.

To better understand the model's decision-making process, we performed a detailed feature importance analysis. This revealed that while most features contribute marginally to the classification, a few stand out as particularly informative. Specifically, features related to the de-reddened H_{E} band, including the flux, the S/N, and respective colour combinations, headed by $Y_{\text{E}} - H_{\text{E}}$, as well as the point-like probability, emerge as the most significant predictors. For a more comprehensive overview of feature contributions, we refer the reader to Appendix A.

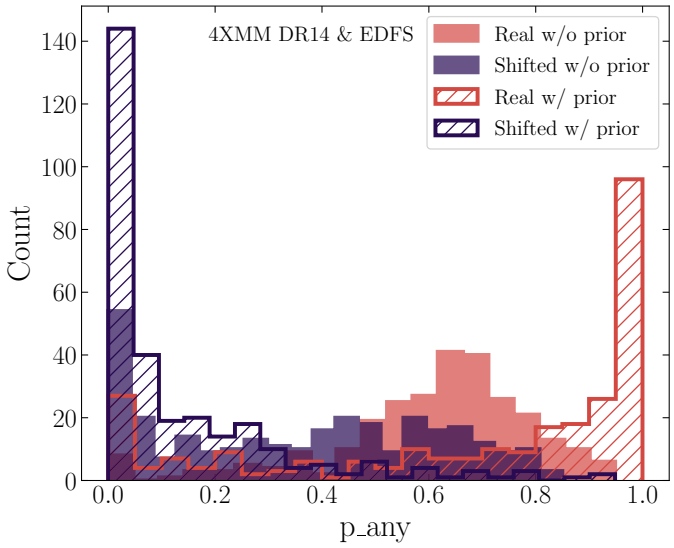

Fig. 4. Example of `p_any`, the probability than an X-ray source has a *Euclid* CTP, showing distributions for both random and real X-ray sources before (filled) and after (hatched) incorporating the photometric prior in `NWAY`. For the random sources, the inclusion of the prior shifts the `p_any` values to lower values, indicating that most associations are due to chance alignments. Conversely, for the real sources, the prior shifts the `p_any` values to higher values, highlighting the increased confidence in the true matches, demonstrating the positive impact of the prior in distinguishing real CTPs from random associations.

4.2. Adding the X-ray emitter prior to `NWAY`

The a-priori probability of an *Euclid* source to be an X-ray emitter, $P_{\text{X-ray}}$, is now incorporated as a prior into the `NWAY` framework to enhance our CTP identification process. To visualise the positive impact of the inclusion of this prior, we plot the distribution of `p_any` both before and after the inclusion of the X-ray emitter prior (see Fig. 4). Incorporating the prior shifts the distribution of `p_any` to higher values, making the identification of true CTPs more reliable. Notably, the inclusion of the prior also changes the respective CTP in about 30% of the cases, indicating that for those sources that are indeed not the CTP after adding the prior, the `p_any` value has been decreased.

In total, we associate 12 645 CTP candidates. Among these, 11 286 (about 90%) sources have `match_flag` == 1, indicating that they have the highest probability `p_i` to be considered reliable CTPs. The remaining candidates, with `match_flag` == 2, represent secondary but plausible matches that are not ruled out entirely. We find 1092 X-ray sources with multiple CTPs, the vast majority of which is made up by XMM-*Newton* and eROSITA with only *Chandra* providing the required positional accuracy for *Euclid* to have few sources with multiple plausible CTPs. While most of the multi-CTP cases are made up of two candidates, a few cases with > 2 CTPs are introduced, predominantly by eROSITA, given its larger positional uncertainty. Notably, only five X-ray sources within the Q1 footprint (see Table 1) lack an association entirely, possibly due to boundary effects where the true CTP falls outside the region covered by the EDFs.

Table 3. CTP sample overview.

X-ray catalogue	X-ray sources	CTPs	AND match_flag == 1	AND in LS10	AND $S/N_r >= 3$	$P_{Gal} < 0.5$	w/ spec-z
4XMM DR14	5241	5885	5239	3774	3711	5486	1122
CSC 2.0	1669	1712	1666	684	669	1625	442
eROSITA DR1	4381	5048	4381	4159	4141	4375	477
Total:	11 291	12 645	11 286	8617	8521	11 486	2044

Notes. (1) X-ray catalogue, (2) number of X-ray sources, (3) number of CTP candidates, (4) unique CTPs with `match_flag==1`, (5) unique CTPs successfully matched to LS10, (6) unique CTPs in LS10 with $S/N_r \geq 3$. The respective number of CTP candidates that we consider to be extragalactic is given in column 7, while the number of candidates with publicly available spectroscopic redshifts is given in column 8.

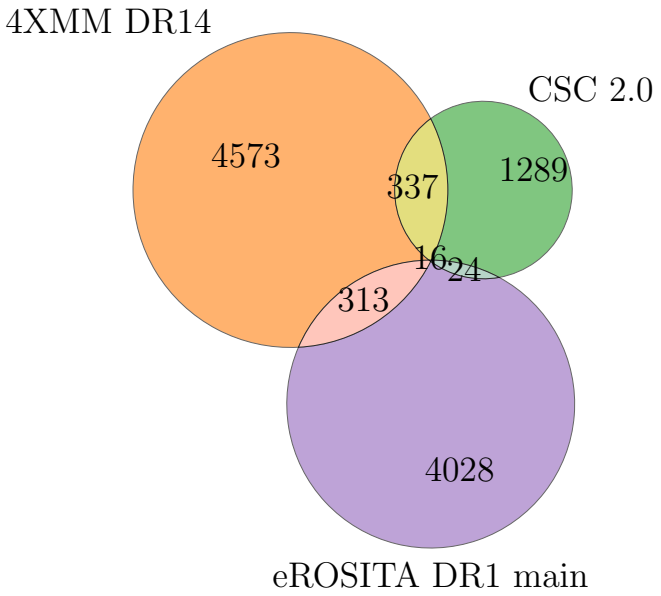

Fig. 5. Venn diagram illustrating the overlap of shared *Euclid* CTPs among the three X-ray samples, 4XMM DR14, CSC 2.0, and eROSITA DR1 main, as listed in Table 3. The diagram shows the distribution of sources that are uniquely or jointly identified by the surveys, with larger overlapping areas indicating stronger agreement among the surveys.

With this catalogue, several scenarios emerge in terms of the relationships between CTPs and X-ray sources.

1. Two X-ray entries from differing surveys are assigned to a single CTP. This scenario suggests but does not confirm the possibility of a single physical source being detected by two different X-ray surveys.
2. Two X-ray entries from the same survey are assigned to a single CTP. Here, we can confidently state that two distinct physical sources are selected, though both are associated with the same *Euclid* ID.
3. Cases where a single *Euclid* ID is linked to multiple entries from e.g., two or even all three X-ray surveys.
4. Two X-ray entries where the same X-ray source, detected by multiple surveys, is matched to distinct *Euclid* CTPs.

Among the surveys, only eROSITA uniformly covers two of the three fields. In contrast, other surveys consist of pointed observations with differing depths and catalogues across distinct bands, meaning sources are not always detected at the same flux levels. As a result, the overlap between catalogues is complex and interpreting source matches becomes challenging. At this stage, gaps in coverage further limit the significance of overlap checks. Keeping this in mind we find 674 pairs which either correspond to case one or two, as well as 16 triplets referring to case three as shown in Fig. 5. We deliberately choose not to quantify case four, as there is currently no definitive way to resolve it with certainty. A breakdown of the CTP sample is given in Table 3.

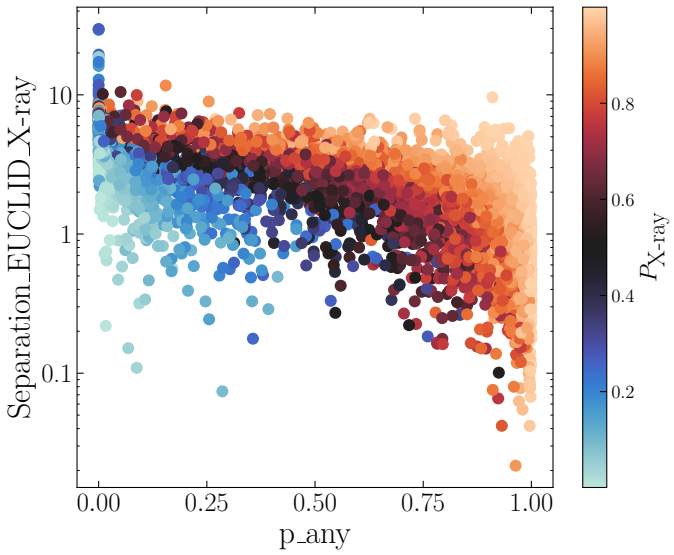

Fig. 6. Relationship between the separation (in arcseconds) between X-ray sources from 4XMM DR14 and their selected CTP as function of `p_any`, colour-coded by $P_{X\text{-ray}}$. The plot highlights that a minimal (or very small) fraction of matches have separations above 10″, with `p_any` enhanced by the probability to be X-ray emitting.

4.3. Purity and completeness

To calibrate a reliable `p_any` cut-off, we perform the `NWAY` procedure (using the same prior) on a duplicate sample of the X-ray sources, referred to as 'randoms'. These randoms are generated by displacing the positions of the X-ray sources to lie beyond the search radius, ensuring that any matches with multiwavelength CTPs are purely coincidental. By comparing the distribution of `p_any` values for both the original X-ray sample and the randoms, we can assess the impact of the prior by examining the two histograms in Fig. 4. The figure shows how the `p_any` value for the randoms is usually lower than for the real sample of X-ray sources, indicating that in a random position in the sky, there are no sources that have the same features of a typical X-ray emitters. For the few sources for which `p_any` remains high, either the prior was not representative enough, or, deeper data in the future will potentially reveal a fainter X-ray source.

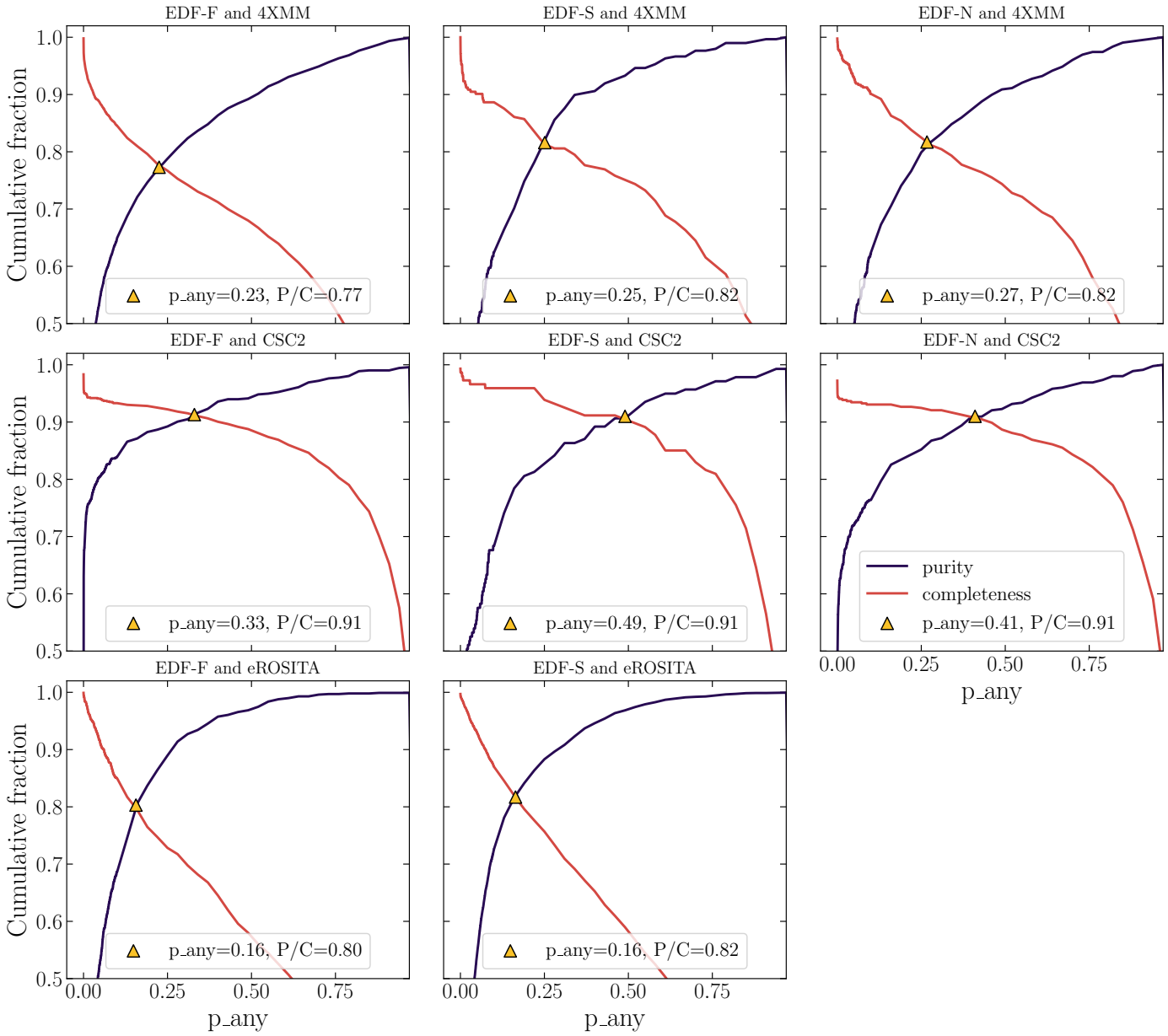

Fig. 7. Purity (red) and completeness (purple) as a function of `p_any` for matches between the different EDFs and the three X-ray catalogues: 4XMM DR14 (top row); CSC 2.0 (middle row); and eROSITA DR1 (bottom row). Based on these figures users can adopt the `p_any` value threshold that enhances purity or completeness, depending on their scientific preference. The intersection point serves as a threshold for the `p_any` selection.

To further assess the impact of incorporating $P_{\text{X-ray}}$ into the `NWAY` procedure, we compare the `p_any` values as a function of the separation distance between the primary (X-ray) and secondary (multi-wavelength) sources. Figure 6 presents the separation between the 4XMM sources and the associated CTP in EDF-F as a function of `p_any`. The sources with a higher probability of being correct also have a high probability of being X-ray emitters, even at larger separation, the latter being mostly smaller than 10″. CTPs of little separation and low `p_any` showcase scenarios of chance alignments where objects appear close but do not show significant $P_{\text{X-ray}}$. Next, we focus on evaluating the purity and completeness of the CTP samples based on how they are sub-selected. In this context, we define completeness as the cumulative fraction of sources with `p_any` higher than a certain value and purity the fraction of sources with `p_any` higher than the value in the random sample. This gives a measure of how often the CTP in the real sample is associated to a CTP only by chance.

Figure 7 shows both purity and completeness for each EDF and X-ray survey as well as the 'sweet spot' for the best trade off between these quantities as a function of `p_any`. Variations in the distributions result from differences in the positional uncertainties of the X-ray surveys and the source densities within both the X-ray data and the corresponding EDF. Depending on the scientific goal, a user interested in creating a catalogue that is extremely complete or pure, is hence free to select sources with a `p_any` beyond a certain threshold. For the rest of the work, we adopt the intersection between the purity and completeness curves as the threshold. In all fields, purity and completeness are at least 80%, with the *Chandra* catalogues unsurprisingly having the most reliable associations, reaching values of about 90%. Interestingly, the impact of the higher spatial resolution of *Chan-*

dra is clear in the EDF-F field, where Fornax, the second richest galaxy cluster of the local Universe is located. In such a dense environment, it is more challenging to identify the correct CTP given the resolution of 4XMM and eROSITA.

To conclude this part, we assess the stability in the method by examining the impact of RF hyper-parameters like minimum leaf size and features per tree. Variations in these parameters mainly shift the intersection of purity and completeness curves along the p_any axis, with smaller leaf sizes enhancing subclass specificity and subtly altering the intersection point.

4.4. Separation and magnitude distribution of CTPs

The distribution of observed X-ray-optical separations, normalised by the X-ray positional uncertainty, is presented in Fig. 8 as a function of the CTP's $Y_{\rm E}$-band magnitude. For a quality-selected sample of p_any > 0.2, this distribution well aligns with the expected Rayleigh distribution for a scale factor of $\sigma = 1$, indicating consistent behaviour with statistical expectations, demonstrating the reliability of the matching process (e.g., Salvato et al. 2022). The bulk of the sources have a mean separation of 1.″22 and $Y_{\rm E} = 20.65$.

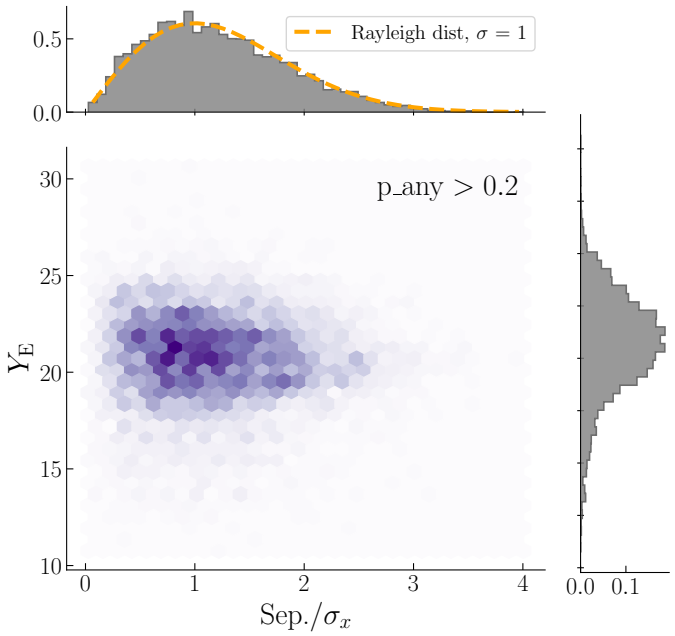

Fig. 8. Separation between the X-ray position and the selected CTP, where the $Y_{\rm E}$ magnitude for sources with CTPs (p_any > 0.2) is plotted against the normalised 1-dimensional positional error of the X-ray sources. The hexagonal bins are colour-coded linearly based on the count of sources within each bin. Marginal histograms show the distribution along the axes, with a linear y-axis scale. The expected $1\,\sigma$ Rayleigh distribution for the normalised separations is overlaid in orange.

5. Characterisation and classification of CTPs

Once the CTPs have been identified, it is essential to categorise the sources in order to study the underlying physical processes and populations. The primary distinction is between extragalactic sources (such as galaxies or faint and bright AGN) and galactic sources (including stars and compact objects). In the following section, we outline the methodology used for classifying the sources and the validation tests conducted to ensure the accuracy of the classification, the results of which are summarised in Table 3.

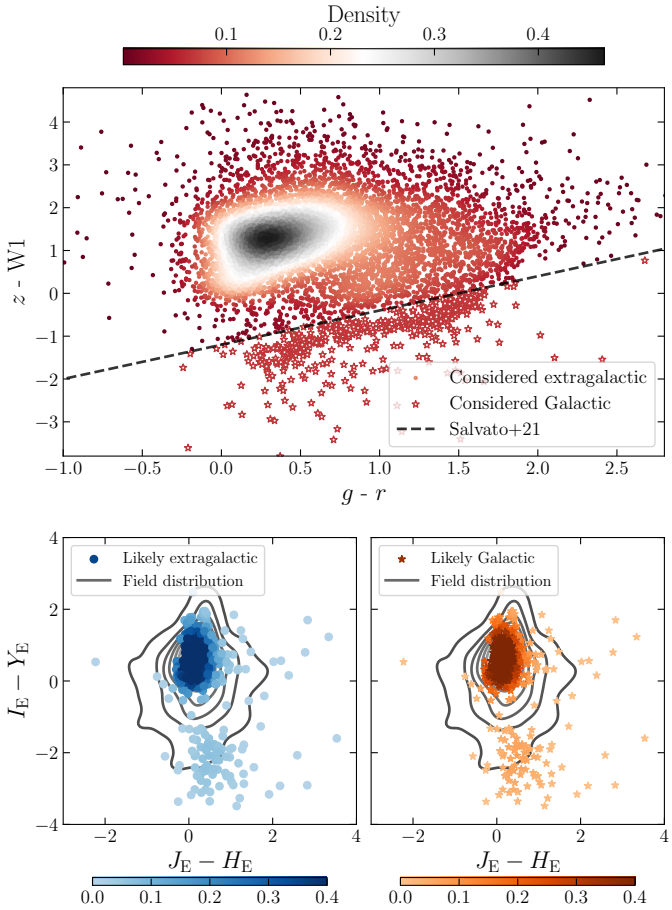

Fig. 9. *Upper row:* Colour-colour plot showing the positional matched *Euclid* CTPs to LS10 sources with 'good' photometry (S/N > 3), adapted from Salvato et al. (2022). This distribution is used to segment sources into Galactic and extragalactic classes. *Lower row: Euclid* colours for extragalactic (left) and Galactic (right) distributions plotted on top of the contours of *Euclid* field sources. The plots confirm that *Euclid* colours cannot differentiate between Galactic and extragalactic sources, since both distributions are very similar.

5.1. Galactic and extragalactic sources

The four *Euclid* bands alone lack the discriminatory power required to reliably separate Galactic from extragalactic sources, given the broadness of the optical filter, where most of the differences within the SED occur. As demonstrated in Euclid Collaboration: Bisigello et al. (2024), no combination of *Euclid*-only photometry achieves satisfactory fractions of purity and completeness for this task. Moreover, the ground-based photometry added to the Q1 catalogues is not completely cross-calibrated at this stage, and differences in quality and bands available differ from field to field. For this reason, we decided to use the photometry available in LS10, providing us with well-calibrated and reasonable depth in *griz* from DECam Legacy Survey observations, including data from the Dark Energy Survey (DES, Dark Energy Survey Collaboration et al. 2016), Beijing-Arizona Sky Survey (BASS, Zou et al. 2017), and the Mayall z-band Legacy Survey (MzLS, Silva et al. 2016), as well as W[1,2,3,4] from

the Near-Earth Object Wide-field Infrared Survey Explorer (NEOWISE, Mainzer et al. 2011; Lang 2014; Meisner et al. 2017). We match the 11 286 CTPs to LS10 using a 1″ positional tolerance and find an association for 68% of our sources, see Table 3. Next, we apply a cut of S/N > 3 in the g, r, z, and W1 bands to minimise the relative impact of photometric uncertainties. The selected sources are then plotted on the $z-$W1 versus $g-r$ colour-colour plane, to distinguish between Galactic and extragalactic objects (see Fig. 9). Using the separation line defined in Salvato et al. (2022), we preliminarily classify sources based on their location relative to the threshold. Objects above the threshold are flagged as extragalactic, while those below are classified as Galactic.

These classifications are then used to create individual subplots (lower panels of Fig. 9), displaying the sources by their classification using only *Euclid* colours. As highlighted in Euclid Collaboration: Bisigello et al. (2024), the Galactic and extragalactic sources trace almost the same feature space, confirming that *Euclid* photometry alone, comprising the I_E, Y_E, J_E, and H_E bands, does not provide sufficient information to reliably distinguish between the two populations.

5.2. Probabilistic classifier approach

To overcome this limitation, we follow the methodology outlined in Sect. 4.1.1, training an RF classifier using the same *Euclid*-only features listed in Table 2. However, this time we label the sample based on the classification derived from the $z-$W1 versus $g-r$ plot, setting Galactic objects (396) to '1' and extragalactic objects (1000) to '0'. Using the trained model, we assign a Galactic or extragalactic label to each *Euclid* CTP, providing a probabilistic classification $P_{\rm Gal}$ for robust downstream analyses.

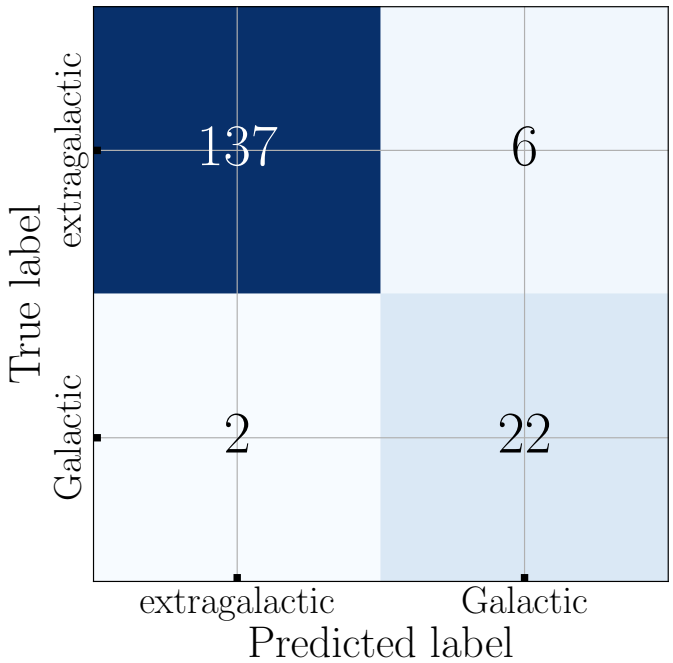

Fig. 10. Confusion matrix from the RF Galactic/extragalactic classifier applied to an independent test set. Sources classified as residing within the MW are labelled as 'Galactic' while field objects are labelled as 'extragalactic'.

We present the respective confusion matrix in Fig. 10 and note a recall of 92%, with a limited fall-out of 4%. For more details on the feature correlations see Appendix A. To further validate the RF performance, we examine the galactic probability distribution ($P_{\rm Gal}$) for the unique CTP candidates sample. Less than 10% of sources have $P_{\rm Gal} > 0.5$, indicating effective separation of Galactic and extragalactic populations. A comparison with the Euclid Collaboration: Matamoro Zatarain et al. (2025) classification reveals that 97% of sources classified as Galactic there, also have $P_{\rm Gal} > 0.5$, confirming good agreement. Additionally, the colour-coding of Fig. 11 reveals that most sources classified as being Galactic make up the bright end of the sample, with the most intense colour gradient surrounding $P_{\rm Gal} = 0.5$ and a couple of sources towards high $P_{\rm Gal}$ interestingly appearing increasingly fainter again, probably due to different populations of stars, subject to their location in the extragalactic sky.

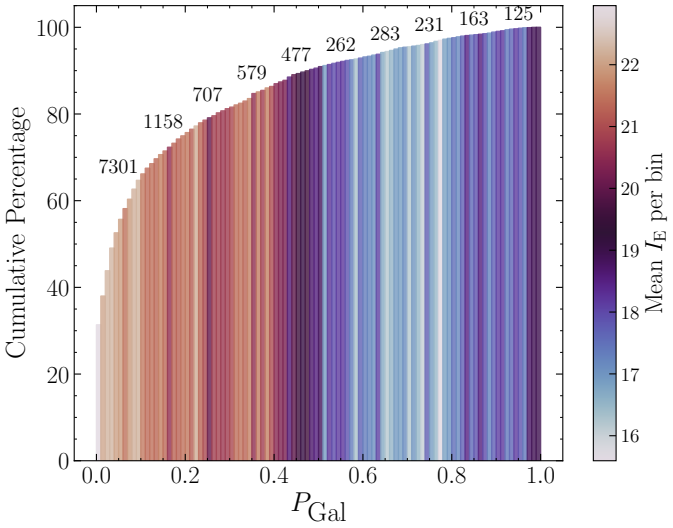

Fig. 11. Cumulative histograms showing the respective percentage of CTPs, as a function of $P_{\rm Gal}$. Values of $P_{\rm Gal} < 0.5$ correspond to sources classified as extragalactic, while values above 0.5 classify them as being Galactic. Only roughly 8% of sources have $P_{\rm Gal} > 0.5$, indicating a predominantly extragalactic population. In addition, each bin of the histogram is coloured by its mean I_E magnitude, while the sum of each set of 10 adjacent bins is printed on top.

6. Redshifts

The catalogues of CTPs we make available in this paper include spectroscopic redshifts (spec-zs), where available, by matching their coordinates to a compilation of publicly available redshifts (Kluge et al. 2024). However, this compilation is rich in duplications, hence the details of the cleaning are described in Sect. 3.1 of Saxena et al. (2024). While spec-zs provide highly accurate distance measurements, they are inherently limited to a subset of typically brighter objects. As a result only 16% of the CTP sample benefits from publicly available spec-z coverage (refer to Table 3).

6.1. Photometric redshifts

To achieve a more complete characterization of the CTPs, photometric redshifts (photo-zs) are essential. However, achieving reliable photo-zs for AGN remains significantly more challenging than for inactive galaxies, despite notable advances in recent years (see Salvato et al. 2019, for a review).

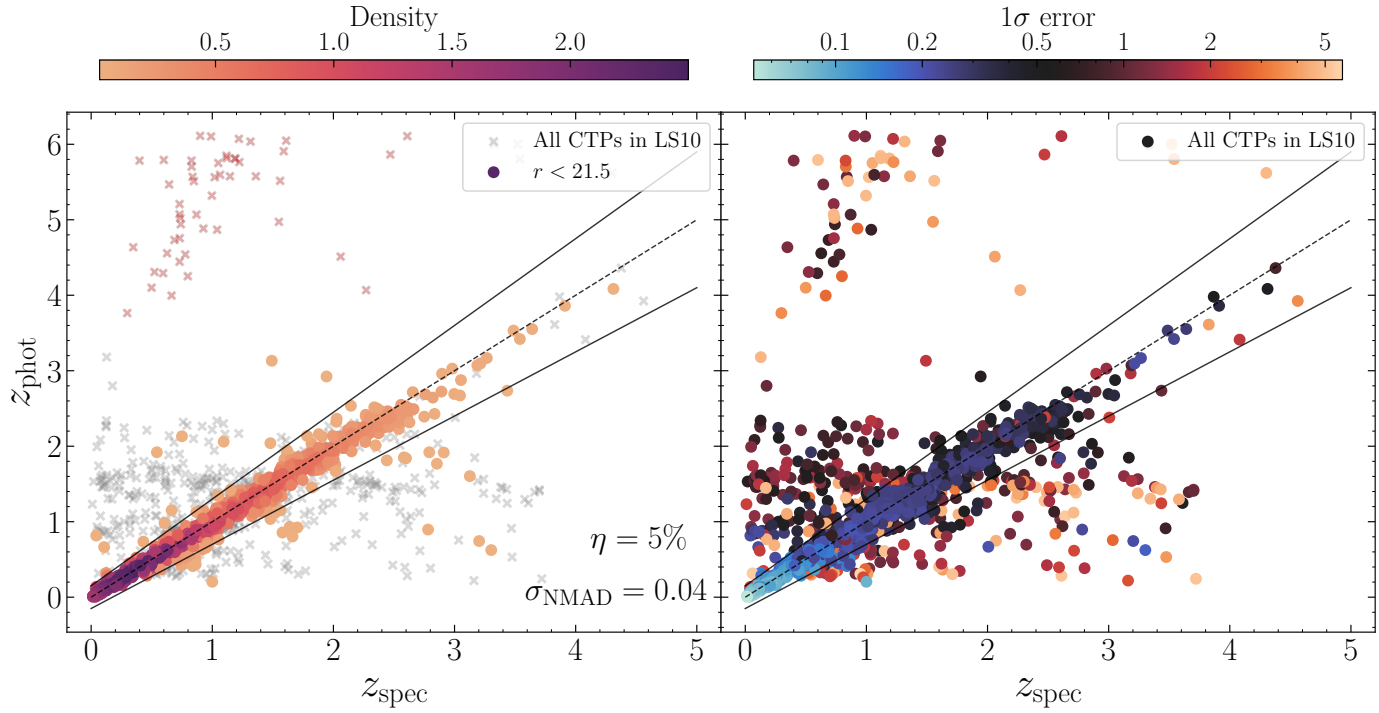

Fig. 12. Photometric redshifts vs. spectroscopic redshifts for all CTPs matched to LS10. *Left:* points are colour-coded according to the density of sources with $r \leq 21.5$. Respective statistics are denoted in the bottom right corner. The sources shaded red at the top left corner are considered catastrophic outliers, with visual inspection denoting them as faint, galaxy-dominated objects with increased uncertainties. *Right:* the same distribution colour-coded by the 1σ error ($z_{\rm phot,1su} - z_{\rm phot,1sl}$). Sources closely following the identity line exhibit significantly lower errors, while outliers are associated with larger errors. This demonstrates how PICZL effectively produces reliable error estimates, accurately reflecting the uncertainty in the photometric redshift measurements. The robustness of these error calculations underscores their importance for interpreting the results.

The primary difficulty lies in the overwhelming emission produced by the accretion onto the SMBH, which often masks the spectral features of the host galaxy, crucial for breaking colour-redshift degeneracies. The current version of photo-zs released for Q1 assumes the sources to be inactive galaxies and does not account for the possible contribution from an active nucleus. The absence of AGN SEDs in the template library makes it difficult to accurately constrain their contributions using photometry alone, resulting in miscalculations of the physical parameters for each source derived indirectly. Instead, studies have demonstrated that incorporating aperture or pixel-based analyses can significantly enhance the accuracy of such photo-z estimates. Consequently, to compute reliable photo-zs for AGN-dominated objects in a dedicated effort, we utilise PICZL (Roster et al. 2024), an ML algorithm that significantly improves photo-z estimation for AGN by directly predicting redshifts from imaging data, eliminating the need for manual feature extraction or additional surveys. Building on its predecessor, CIRCLEZ (Saxena et al. 2024), which analysed aperture-based photometric variations, PICZL advances to pixel-level resolution, leveraging the raw images for improved precision. As a result, for sources bright enough to successfully be matched to the LS10 catalogue, we are able to produce reliable photo-zs (refer to Table 3). This is possible since the training sample constructed for PICZL is formed mostly by X-ray selected AGN detected in LS10, enabling us to use the same model. As in the original work, the uncertainty of the photo-zs in terms of 1σ error, increases with the faintness of the sources (see Roster et al. 2024, for more details).

For all EDF CTPs of an X-ray source detected in LS10, PICZL provides full redshift posterior distributions (PDZ) derived from de-reddened calibrated images in the g, r, i, and z bands, supplemented by $W1$, $W2$, $W3$, and $W4$ catalogue-based aperture photometry without imposing any S/N cuts. The method is agnostic to the morphological classification of the source, applying equally to extended and point-like objects. As output, PICZL provides the dominant mode of the PDZ as a point prediction, along with uncertainties quantified as 1σ and 3σ confidence intervals. Notably, we compute photo-zs also for those CTPs matched to LS10, which we believe to be Galactic. This approach accounts for the inherent uncertainty in the probabilities produced by our model and classification threshold. To ensure flexibility for users, we include both classifications and photo-

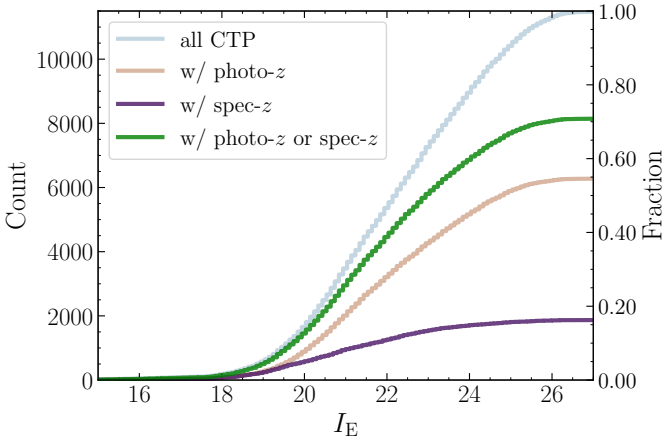

Fig. 13. Cumulative histogram showing the count of sources with spectroscopic and/or photometric redshifts in relation to all CTPs with $P_{\rm Gal} \leq 0.5$ as a function of their $I_{\rm E}$ magnitude.

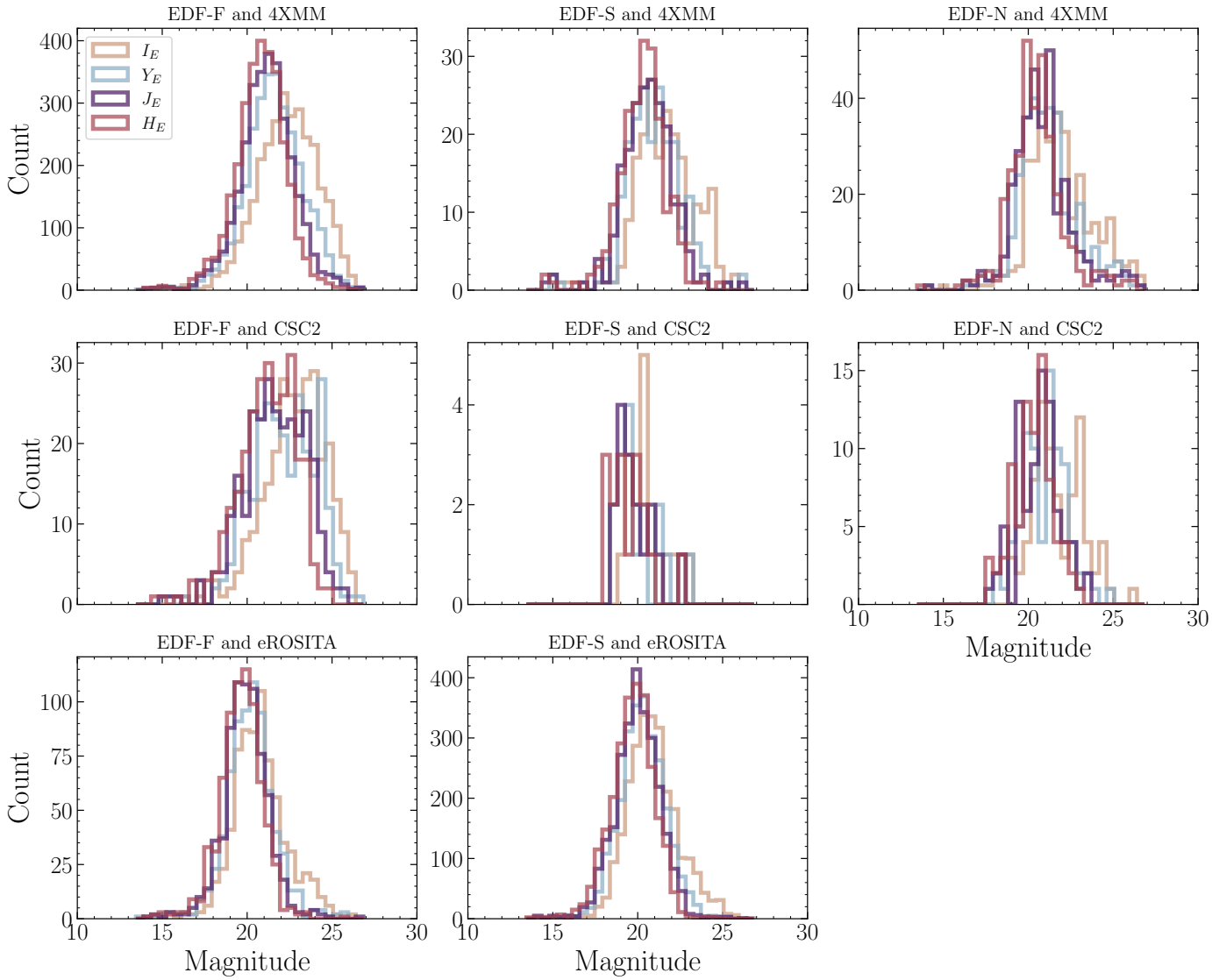

Fig. 14. Distribution of source counts for each combination of EDF (EDF-F, EDF-S, and EDF-N) and X-ray survey (4XMM on top row, CSC 2.0 in the middle one, and eROSITA DR1 in the bottom panels). Each plot presents the histograms corresponding to the four *Euclid* bands, depicting the count of sources as a function of magnitude.

z estimates in the released catalogue (see Sect. 8). This allows users to tailor their selection criteria to their preferences while retaining access to the full set of photo-z values.

6.2. Photo-z quality

To evaluate the reliability of our photo-z estimates, we employ standard metrics commonly implemented in the literature, including (a) the accuracy $\sigma_{\rm NMAD}$ as a measure of the scatter between the prediction and truth values of the sample, defined as

$$\sigma_{\rm NMAD} = 1.4826 \cdot \text{median}\left[\frac{|z_{\rm phot} - z_{\rm spec}|}{(1 + z_{\rm spec})}\right]; \quad (7)$$

and (b) the fraction of outliers, η, which quantifies the proportion of sources whose redshift estimates deviates significantly from their corresponding spectroscopic redshift. Specifically, this is defined as the fraction of objects for which

$$\eta = \frac{|z_{\rm phot} - z_{\rm spec}|}{(1 + z_{\rm spec})} > 0.15\,. \quad (8)$$

We evaluated the performance of the photo-zs by comparing them to the spec-zs, as shown in Fig. 12. For the subsample of sources with $r < 21.5$, which corresponds to the brighter and more reliable sources in our data set, we find that the fraction of outliers is approximately 5%, with a $\sigma_{\rm NMAD}$ of roughly 0.04 as opposed to $\eta = 22.5\%$ and $\sigma_{\rm NMAD} = 0.065$ observed for the entire sample. Additionally, the catastrophic outliers at $z_{\rm phot} > 4$ are faint, galaxy-dominated objects ($r > 24$) with large photometric errors in LS10. In scientific studies involving photometric redshifts, it is crucial to account for such uncertainties and in turn, photometric redshift algorithms should therefore make sure to provide reliable errors. `PICZL` achieves this effectively as discussed in detail in Roster et al. (2024). In the right panel of Fig. 12 this is evidenced by the smaller errors closely tracing the identity line, while larger errors appropriately account for sources of uncertainty.

In Fig. 13, we present the cumulative distribution of CTP $I_{\rm E}$ band magnitudes along with the respective fractions of sources with spectroscopic and/or and photometric redshifts. The figure reveals that the sample is almost complete in redshift up to

around $\sim I_E \leq 21$. For fainter sources, photo-z estimation is either not possible due to the limited number of photometric data points and significant errors, or the source, though clearly detected in *Euclid*, is not visible in LS10 due to its shallower depth. In the future, when we have upgraded PICZL to be applied to *Euclid* images and have integrated data from the Legacy Survey of Space and Time (LSST; Ivezic et al. 2019), photometric redshifts for AGN in *Euclid* will dramatically improve.

7. Properties of the CTP sample

Having successfully selected, classified, and vetted our CTPs, we now turn to an analysis of their properties. From this point forward, we refer to CTPs as those sources meeting the criteria of $P_{\rm Gal} \leq 0.5$ and p_any> 0.05. This refined selection yields a total of 9294 sources from the initial 11 286 entries having match_flag=1.

Figure 14 illustrates the magnitude distribution of our CTPs, grouped by the match between EDFs and the corresponding X-ray survey (4XMM, CSC2, and eROSITA DR1, respectively). The 4XMM and CSC 2.0 distributions show their ability to detect fainter X-ray sources, which correlates with the identification of fainter optical CTPs. In contrast, the eROSITA DR1 distributions exhibit brighter median magnitudes, consistent with the shallowness of the survey (see Fig. 2). Additionally, the figure suggests a possible bimodal distribution at the faint end in the optical band for both 4XMM and CSC 2.0, at least in EDF-N and EDF-S. The majority of ources in the second, faint peak of the distribution show X-ray fluxes $F_{(0.5-2\,\rm keV)} \leq 10^{-14.5}$ erg cm^{-2} s^{-1}, with no obvious drop off in p_any, and the distribution will be studied further in other papers.

7.1. Colour-redshift relation

Redshifts, spectroscopic and photometric, are available for 79% of the CTPs, allowing us to analyse their *Euclid* colours as function of redshift, as shown in Fig. 15. The colour-coded kernel density is plotted along the y-axis dimension within each bin, providing a visual trace of how the physical colours of the CTP sample vary as a function of redshift.

A notable feature in the data is the detection of the Balmer break at $z \simeq 1.3$, particularly prominent in colours including the I_E filter. Unsurprisingly, NIR-only colour combinations display relatively few discernible features (compare e.g., figure 7 in Temple et al. 2021). As iterated before, the *Euclid* filters alone lack the fidelity to catch variations in the SED of sources, a caveat that we will be able to overcome in combination with upcoming surveys, especially LSST.

7.2. X-ray luminosities

For the rest of the analysis, we restrict the CTP sample to those 7345 extragalactic sources with a soft X-ray flux S/N ≥ 2 in order to reduce potential spurious X-ray detection. In Fig. 16, we observe a clear distinction between pointed observations taken with XMM-*Newton* and *Chandra* at various depths versus the homogenous all-sky coverage provided by eROSITA. The complete coverage of eROSITA results in a tighter correlation between luminosity and redshift, despite the presence of a few points away from the general trend, which have low S/N (thus indicating potential spurious sources). Another reason for their offset from the general trend could be an incorrect photometric redshift. On the other hand, XMM-*Newton* and *Chandra* catalogues include a mixture of pointed observations resulting in a less smooth distribution between redshift and luminosity.

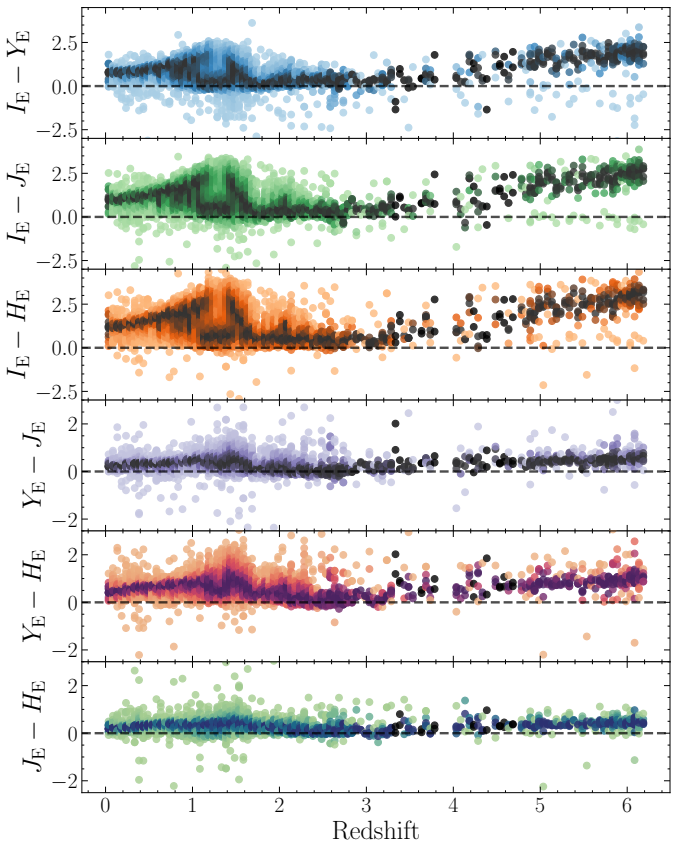

Fig. 15. Colour-redshift relation for all *Euclid* band combinations. Each panel is divided into redshift windows, with the density of points within each bin colour-coded along the dimension of the y-axis, illustrating spectral features in the SED.

In all three panels, we indicate with open circle sources with low S/N$_r$, potentially corresponding to those highlighted red in the left panel of Fig. 12, representing examples of increased redshift uncertainties. Notably, most of the results shown, focus on objects with redshifts of $z < 4$. Sources with higher redshifts, while present, should be approached with caution due to potential inaccuracies. However, the future availability of LSST photometry will enable the exploration of this parameter regime by probing fainter sources with smaller errors, thus improving the reliability of redshift estimates for these populations.

In studies such as that of Georgakakis & Nandra (2011), AGN are typically defined as sources with X-ray luminosities exceeding $L_{(2-10\,\rm keV)} \geq 10^{42}$ erg s^{-1}, since normal galaxies may be an important source of contamination below this limit (Lehmer et al. 2012; Aird et al. 2015). However, it is important to note that this threshold was established based on pencil-beam surveys, suggesting that it should be revisited now that wide-area surveys and deep optical data are accessible. X-ray luminosities of AGN in the soft X-ray band (0.5 – 2 keV) can vary significantly, depending on the AGN type and redshift. In literature, values can range from $L_{(0.5-2\,\rm keV)} \geq 10^{41} - 10^{46}$ erg s^{-1} or even less when considering low-luminosity AGN (Hasinger et al. 2005; Ebrero et al. 2009; Civano et al. 2012; Kawamuro et al. 2013). Applying the criterion of $L_{(0.5-2\,\rm keV)} > 10^{41}$ erg s^{-1}, we classify 6243 out of the 6295 sources with computed X-ray luminosities as AGN.

A more inclusive approach is presented in Georgakakis et al. (2007) for example, where X-ray detected starburst galaxy can-

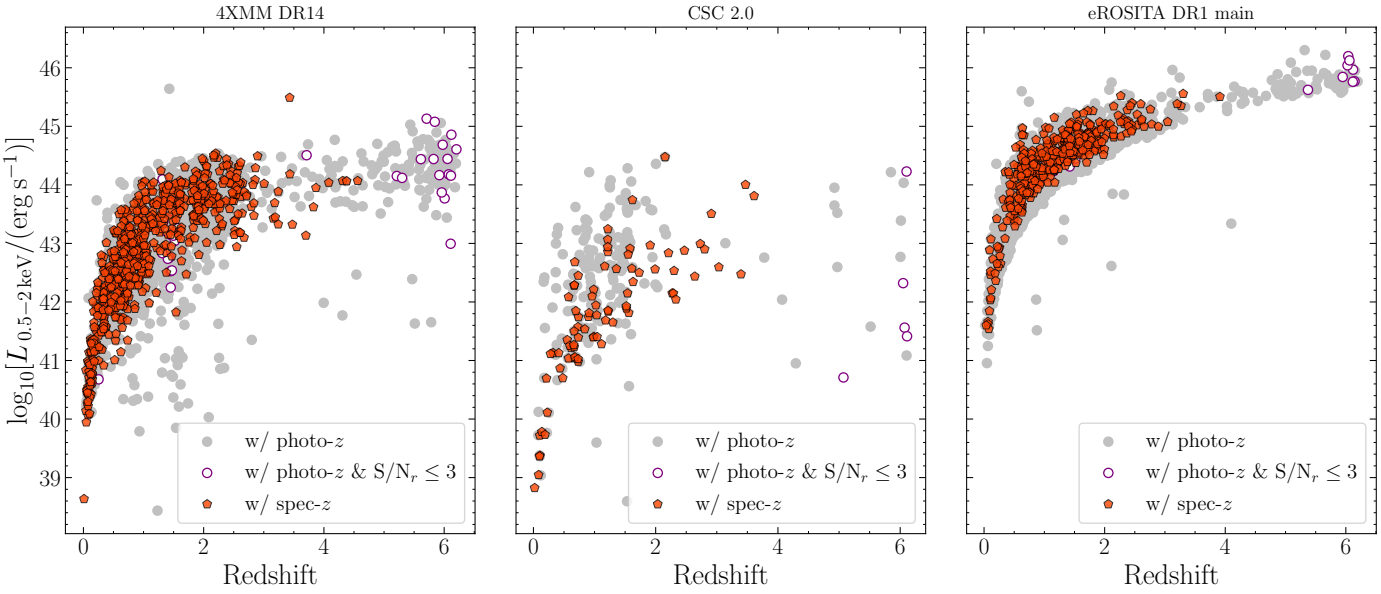

Fig. 16. X-ray luminosity as a function of redshift for the different surveys: 4XMM DR14 (left), CSC 2.0 (centre), and eROSITA DR1 main, (right). Grey circles represent sources with photometric redshifts, while orange pentagons indicate sources with spectroscopic redshifts. Less reliable photometric redshifts of S/N$_r \leq 3$ in LS10 are highlighted by a purple outline.

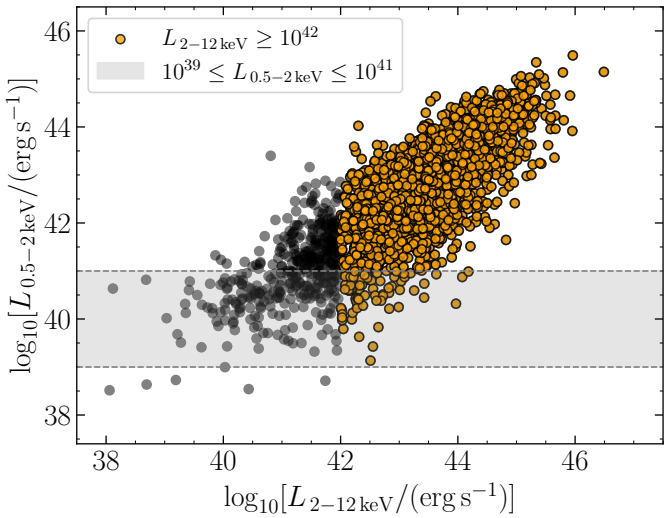

Fig. 17. Scatter plot of soft X-ray luminosities versus hard X-ray luminosities for sources in the 4XMM-DR14 sample. Sources classified as AGN based on their hard-band luminosities are highlighted. Using this classification, we establish a corresponding threshold in soft-band luminosity.

didates, though more likely in case of *Chandra* as opposed to eROSITA (Kyritsis et al. 2025), can represent about 20% of the X-ray source population in the luminosity interval $L_{(2-10\,\mathrm{keV})} \geq 10^{40} - 10^{42}\,\mathrm{erg\,s^{-1}}$. This fraction is also likely to be an upper limit because some of the galaxy candidates may turn out to be low–luminosity AGN, such that distinguishing between these sources can be challenging. Using our sources from XMM-*Newton*, where both soft and hard (2 – 12 keV)[6] band fluxes are available, we show that, to retain all sources in this parent catalogue that are classified as AGN using the hard band, a soft-band luminosity threshold of $L_{(0.5-2\,\mathrm{keV})} \geq 10^{39}\,\mathrm{erg\,s^{-1}}$ is required (refer to Fig. 17). Given the results of both all-sky and pencil beam surveys, at soft luminosities in the range $10^{39}-10^{41}\,\mathrm{erg\,s^{-1}}$, AGN still appear to represent the dominant population. Nonetheless, future studies are required to determine the nature of these low-luminosity AGN at soft energies. Applying this more inclusive threshold defined in Fig. 17 to our extragalactic CTP sample, 6292 of the 6295 sources that we were able to compute X-ray luminosities for, meet the AGN definition criterion.

[6] We assume that at zero order, the luminosities between (2 – 10) and (2 – 12) keV are approximately the same.

7.3. AGN type

In Fig. 18, we plot the respective Y_{E}-band magnitudes as a function of the soft X-ray fluxes for all CTPs classified as extragalactic. We add the |X/O| = 1 lines (Maccacaro et al. 1988), which highlight the typical AGN locus (see also e.g., Salvato et al. 2011; Civano et al. 2012), defined as

$$\mathrm{X/O} = \log_{10}(F_{\mathrm{x}}/F_{\mathrm{opt}}) = \log_{10}\left(\frac{F_x}{\mathrm{erg\,cm^{-2}\,s^{-1}}}\right) \cdot \frac{m_{\mathrm{opt}}}{2.5} + C\,, \quad (9)$$

where F_{x} is the X-ray flux in a given energy range, m_{opt} and C correspond to the magnitude and a constant which both depend on the specific filter used in the optical observations. For Y_{E} we find $C = 5.53$. To further assess the type of our sources, we colour-code the plots in the bottom row of Fig. 18 by the X-ray luminosity and the top row by hardness ratio (Park et al. 2006; Cappelluti et al. 2007; Salvato et al. 2008), defined as

$$\mathrm{HR} = \frac{F_{\mathrm{hard}} - F_{\mathrm{soft}}}{F_{\mathrm{hard}} + F_{\mathrm{soft}}}\,, \quad (10)$$

where a negative HR value indicates (type I) unobscured sources, whereas a positive HR value suggests harder, likely obscured (type II) sources. Therefore, we include fluxes from the hard X-ray band where available. Specifically, we consider fluxes from the 2.0 – 4.5 keV range for 4XMM DR14, the 2.0 – 7.0 keV range for *Chandra*, and the 2.3 – 5.0 keV energy range for eROSITA DR1. This ensures as much consistency as possible

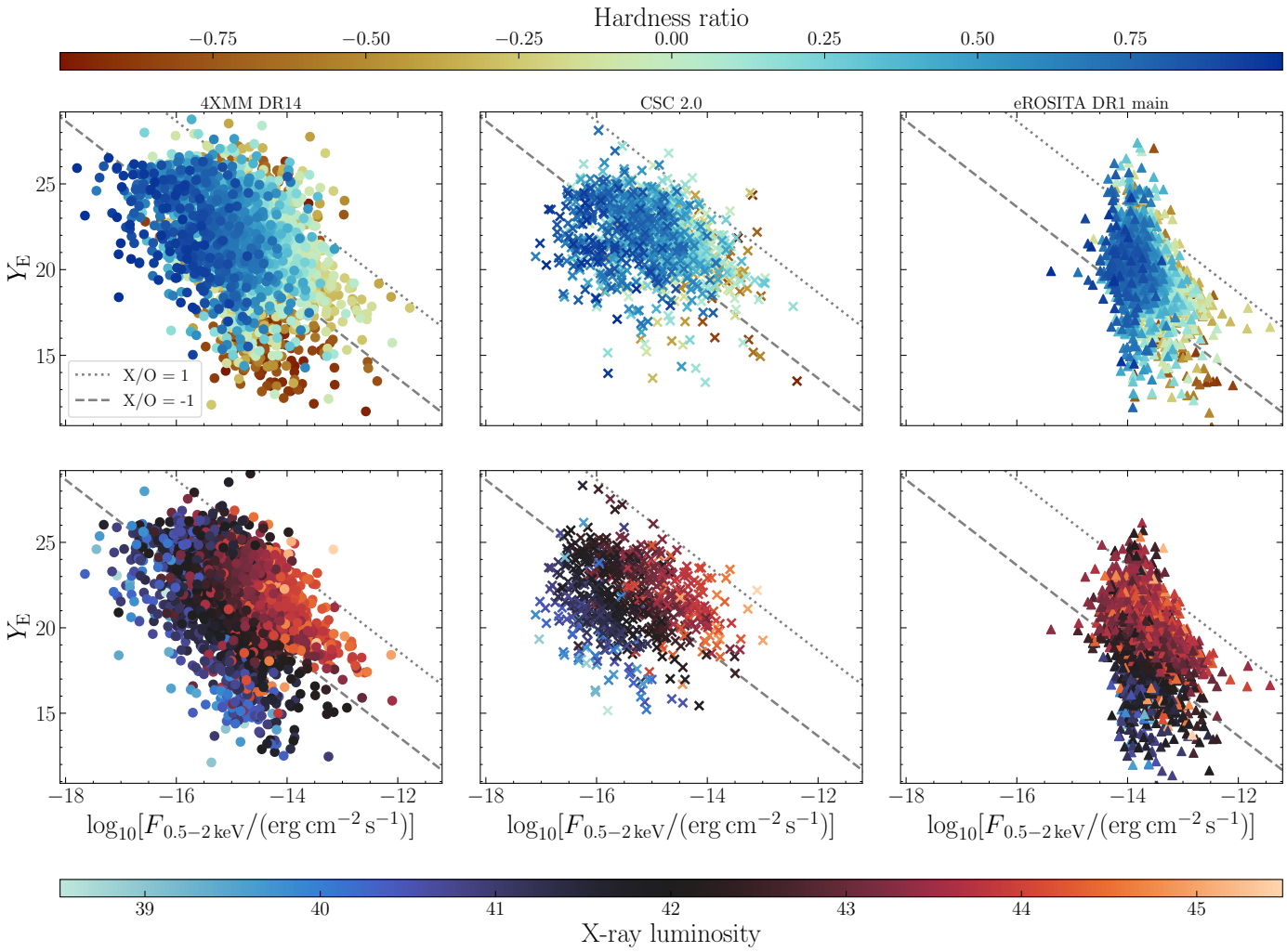

Fig. 18. Distribution of the Y_E magnitude as a function of soft X-ray flux for the three catalogues studied in this work: 4XMM DR14 (left), and CSC 2.0 (centre) and eROSITA DR1 main (left). In each subplot, the dashed lines indicate the $|X/O| = 1$ trend, with sources lying between the lines ($|X/O| < 1$) being usually identified as AGN. The scatter points are colour-coded by their respective hardness ratio (top) and X-ray luminosity (bottom), when available. The markers are plotted in order of increasing hardness ratio.

across the different surveys, allowing us to utilise similar energy bands for comparison and analysis.

Since the markers in Fig. 18 are plotted in order of increasing hardness ratio, many sources in the background are being covered up and predominantly fall within the X/O boundaries, classifying them as bright, unobscured type I sources, with different populations visible for every X-ray survey. This trend is most pronounced for eROSITA, where the distribution is more concentrated within the boundaries. A similar pattern is observed for XMM-*Newton*, though it includes a population of very soft sources lying below the X/O boundaries, potentially corresponding to starburst galaxies. For *Chandra*, the general trend also holds; however, there is an additional presence of very hard sources overlapping with very soft ones below the X/O boundary, particularly in the bright optical and faint X-ray regime. The majority of these outliers are sources with $S/N \leq 3$ in the soft X-ray band, suggesting that at least some of them may be spurious detections. It is also plausible that these sources are intrinsically variable, suggesting that they were observed in different states of appearance. Overall, our distribution follows the findings of Merloni et al. (2014), which show that only approximately 80% of AGN selected by their SED, spectral features and HR, match their expected type I/II class.

8. Release of the catalogue

The catalogue containing the CTPs to the point-like X-ray sources in the EDFs and their properties are available through CDS/Vizier[7]. A detailed description of the columns and their content is provided in Appendix B. The catalogue includes unique identifiers for all relevant surveys as well as the basic X-ray and *Euclid* properties (columns 1 – 13). For the full list of available columns, please refer to the original catalogues introduced in Sect. 3 and e.g., Euclid Collaboration: McCracken et al. (2025); Euclid Collaboration: Polenta et al. (2025); Euclid Collaboration: Romelli et al. (2025). Columns 14 – 24 present the results of the CTP association, followed by key parameters derived from `NWAY`. Photometric data from LS10 are reported in columns 25 – 28. Spectroscopic information, when available, is included in columns 29 – 33. Lastly, the photometric redshift parameters from the `PICZL` algorithm, as well as quantities computed with such, are listed in columns 34 – 40.

[7] https://vizier.cds.unistra.fr

9. Conclusions and outlook

In this paper we have presented the procedure adopted for the identification, classification, and study of the *Euclid* CTPs to the point-like sources selected from XMM-*Newton*, *Chandra*, and eROSITA X-ray, detected in Q1. We summarise the most important results in the following.

- Utilising `NWAY` (Salvato et al. 2018), supplemented by a prior on X-ray emission, based on properties of a 4XMM DR11, and CSC 2.0 training sample, we achieved highly accurate CTP identifications relying on *Euclid* photometry only (see Sect. 4). Randomising the X-ray position and repeating the same procedure for the association, we quantify for each X-ray source the probability of chance associations. Users will be able to create subsamples of CTPs of desired purity and completeness by applying more restrictive or inclusive `p_any` (the probability of an X-ray source having a CTP) cuts (see Fig. 7).
- Altogether, we identify 12 645 CTPs, with only about 10% of the sources having more than a single possible CTP, mostly in the 4XMM and eROSITA surveys, due to their larger positional uncertainties, compared to *Chandra*. We attribute this performance to the availability of extensive X-ray detected samples with secure CTPs, and deep, homogenised multiwavelength photometry spanning optical to MIR wavelengths, enabling robust SED construction for training. Further enhancements in expanding to broader multiwavelength coverage will improve the quality of CTP identification, particularly with *Euclid* DR1 in mind.
- We trained a RF algorithm to classify objects as Galactic or extragalactic using solely *Euclid* photometry in Sect. 5. We previously trained on a sample of secure Galactic/extragalactic sources detected in LS10, using a $g-r$ over $z-\mathrm{W1}$ thresholds, as presented in Salvato et al. (2022), effectively breaking the degeneracy in classification that arises when relying on *Euclid* photometry alone (see Euclid Collaboration: Bisigello et al. 2024). We validate these classifications by comparing to Euclid Collaboration: Matamoro Zatarain et al. (2025).
- We also added spectroscopic redshifts for 16% of the CTP sample using publicly available data. For the 76% of the sample detected in LS10, we computed photometric redshifts using `PICZL` (Roster et al. 2024), reaching up to $z \approx 6$, although at these high redshifts the values are associated with large uncertainties. With all these redshifts, we investigated the colour-redshift relation of our sample in addition to computing their X-ray luminosities (refer to Sect. 6). We find that almost all of our CTPs pass the threshold to be considered an AGN, with most of them appearing as soft, bright, and unobscured type I sources.
- As the primary outcome of this paper, we present the CTP catalogue, which includes a wealth of information such as IDs, basic X-ray properties, `NWAY` outputs, classification probabilities, and redshift data (see Sect. 8). By providing probabilities for all applicable sample characteristics, we ensure users have the flexibility to make informed selections tailored to their specific scientific goals, without being constrained by predefined thresholds or assumptions.

The RF models used for the identification of the CTPs and their classification into Galatic/extragalactic, can be applied blindly to the entire Q1 catalogue. For each source, they provide the probability of being an X-ray emitter, as well as an extragalactic source, despite the fact of not having been detected by any of the three X-ray surveys yet. Consequently, as illustrated in Figure Fig. 19, limiting the selection of Q1 sources to those with $P_{\text{X-ray}} > 0.8$ and $P_{\text{Gal}} > 0.2$, while excluding *Euclid* sources classified as CTPs in this study, yields a final sample of 135 303 objects. Notably, approximately 400 of these have been successfully cross-matched geometrically with the little red dots sample introduced by Euclid Collaboration: Bisigello et al. (2025), predominantly occupying the bright end of the magnitude distribution. A forthcoming paper will explore the multi-wavelength nature of likely extragalactic high $P_{\text{X-ray}}$ sources that remain undetected in current X-ray surveys.

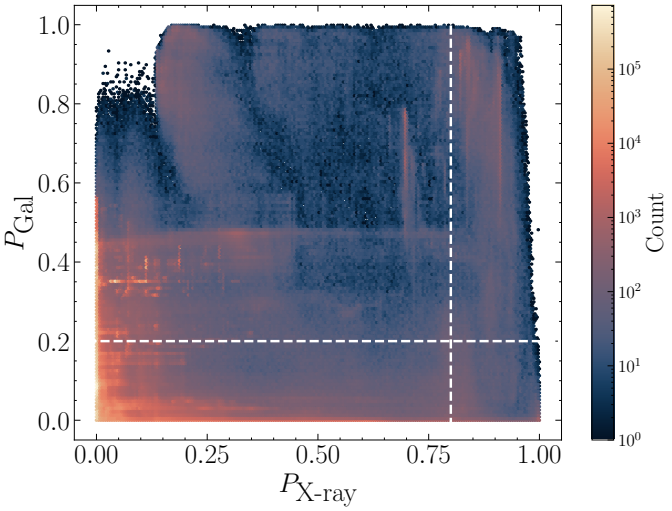

Fig. 19. Hexbin plot illustrating the relationship between the probability of being an X-ray emitter and the probability of being Galactic for all sources in Q1. The plot is colour-coded by the logarithmic kernel density. Orientation lines are included at an X-ray probability of 0.8 and a Galactic probability of 0.2.

Acknowledgements. WR and MS acknowledge DLR support (Foerderkennzeichen 50002207). This work has benefited from the support of Royal Society Research Grant RGS\R1\231450. This research was supported by the International Space Science Institute (ISSI) in Bern, through ISSI International Team project N. 23-573 “Active Galactic Nuclei in Next Generation Surveys”. BL and FR acknowledge the support from the INAF Large Grant "AGN and Euclid: a close entanglement" Ob. Fu. 01.05.23.01.14. This research has made use of data obtained from the Chandra Source Catalog provided by the Chandra X-ray Center (CXC), and the 4XMM XMM-Newton serendipitous source catalogue compiled by the XMM-Newton Survey Science Centre consortium. This work is based on data from eROSITA, the soft X-ray instrument aboard SRG, a joint Russian-German science mission supported by the Russian Space Agency (Roskosmos), in the interests of the Russian Academy of Sciences represented by its Space Research Institute (IKI), and the Deutsches Zentrum für Luft- und Raumfahrt (DLR). The SRG spacecraft was built by Lavochkin Association (NPOL) and its subcontractors, and is operated by NPOL with support from the Max Planck Institute for Extraterrestrial Physics (MPE). The development and construction of the eROSITA X-ray instrument was led by MPE, with contributions from the Dr. Karl Remeis Observatory Bamberg & ECAP (FAU Erlangen-Nuernberg), the University of Hamburg Observatory, the Leibniz Institute for Astrophysics Potsdam (AIP), and the Institute for Astronomy and Astrophysics of the University of Tübingen, with the support of DLR and the Max Planck Society. The Argelander Institute for Astronomy of the University of Bonn and the Ludwig Maximilians Universität Munich also participated in the science preparation for eROSITA. Based on data from UNIONS, a scientific collaboration using three Hawaii-based telescopes: CFHT, Pan-STARRS, and Subaru `www.skysurvey.cc` and data from the Dark Energy Camera (DECam) on the Blanco 4-m Telescope at CTIO in Chile `https://www.darkenergysurvey.org`. This work uses results from the ESA mission *Gaia*, whose data are being processed by the Gaia Data Processing and Analysis Consortium `https://www.cosmos.esa.int/gaia`. The Euclid Consortium acknowledges the European Space Agency and a number of agencies and institutes that have supported the development of *Euclid*, in particular the Agenzia Spaziale Italiana, the Austrian Forschungsförderungsgesellschaft funded through BMK, the Belgian Science Policy, the Canadian Eu-

clid Consortium, the Deutsches Zentrum für Luft- und Raumfahrt, the DTU Space and the Niels Bohr Institute in Denmark, the French Centre National d'Etudes Spatiales, the Fundação para a Ciência e a Tecnologia, the Hungarian Academy of Sciences, the Ministerio de Ciencia, Innovación y Universidades, the National Aeronautics and Space Administration, the National Astronomical Observatory of Japan, the Netherlandse Onderzoekschool Voor Astronomie, the Norwegian Space Agency, the Research Council of Finland, the Romanian Space Agency, the State Secretariat for Education, Research, and Innovation (SERI) at the Swiss Space Office (SSO), and the United Kingdom Space Agency. A complete and detailed list is available on the *Euclid* web site (www.euclid-ec.org). This work has made use of the *Euclid* Quick Release (Q1) data from the *Euclid* mission of the European Space Agency (ESA), 2025, https://doi.org/10.57780/esa-2853f3b. This work has made use of CosmoHub, developed by PIC (maintained by IFAE and CIEMAT) in collaboration with ICE-CSIC. CosmoHub received funding from the Spanish government (MCIN/AEI/10.13039/501100011033), the EU NextGeneration/PRTR (PRTR-C17.I1), and the Generalitat de Catalunya.

References

Aird, J., Coil, A. L., Georgakakis, A., et al. 2015, MNRAS, 451, 1892
Aird, J., Nandra, K., Laird, E. S., et al. 2010, MNRAS, 401, 2531
Ananna, T. T., Salvato, M., LaMassa, S., et al. 2017, ApJ, 850, 66
Assef, R. J., Stern, D., Kochanek, C. S., et al. 2013, ApJ, 772, 26
Baldwin, J. A., Phillips, M. M., & Terlevich, R. 1981, PASP, 93, 5
Bettoni, D., Falomo, R., Kotilainen, J. K., Karhunen, K., & Uslenghi, M. 2015, MNRAS, 454, 4103
Boller, T., Freyberg, M. J., Trümper, J., et al. 2016, A&A, 588, A103
Bongiorno, A., Mignoli, M., Zamorani, G., et al. 2010, A&A, 510, A56
Bovy, J., Myers, A. D., Hennawi, J. F., et al. 2012, ApJ, 749, 41
Brandt, W. N. & Hasinger, G. 2005, ARA&A, 43, 827
Brescia, M., Cavuoti, S., & Longo, G. 2015, MNRAS, 450, 3893
Brunner, H., Liu, T., Lamer, G., et al. 2022, A&A, 661, A1
Brusa, M., Civano, F., Comastri, A., et al. 2010, ApJ, 716, 348
Buchner, J., Georgakakis, A., Nandra, K., et al. 2015, ApJ, 802, 89
Budavári, T. & Szalay, A. S. 2008, ApJ, 679, 301
Cappelluti, N., Hasinger, G., Brusa, M., et al. 2007, ApJS, 172, 341
Cavuoti, S., Brescia, M., D'Abrusco, R., Longo, G., & Paolillo, M. 2014, MNRAS, 437, 968
Chen, H., Lundberg, S. M., & Lee, S.-I. 2022, Nature Communications, 13
Cielo, S., Bieri, R., Volonteri, M., Wagner, A. Y., & Dubois, Y. 2018, MNRAS, 477, 1336
Civano, F., Elvis, M., Brusa, M., et al. 2012, ApJS, 201, 30
Cooper, N., Dainotti, M. G., Narendra, A., Liodakis, I., & Bogdan, M. 2023, MNRAS, 525, 1731
Cuillandre, J.-C., Bolzonella, M., Boselli, A., et al. 2024, A&A, accepted, arXiv:2405.13501
Daoutis, C., Kyritsis, E., Kouroumpatzakis, K., & Zezas, A. 2023, A&A, 679, A76
Dark Energy Survey Collaboration, Abbott, T., Abdalla, F. B., et al. 2016, MNRAS, 460, 1270
De Breuck, C., van Breugel, W., Röttgering, H., & Carilli, C. 2002, in ASP, Vol. 284, IAU Colloq. 184: AGN Surveys, ed. R. F. Green, E. Y. Khachikian, & D. B. Sanders, 275
Delvecchio, I., Smolčić, V., Zamorani, G., et al. 2017, A&A, 602, A3
Dey, A., Schlegel, D. J., Lang, D., et al. 2019, AJ, 157, 168
Dey, B., Andrews, B. H., Newman, J. A., et al. 2022, MNRAS, 515, 5285
Donley, J. L., Koekemoer, A. M., Brusa, M., et al. 2012, ApJ, 748, 142
Ebrero, J., Carrera, F. J., Page, M. J., et al. 2009, A&A, 493, 55
Elvis, M., Wilkes, B. J., McDowell, J. C., et al. 1994, ApJS, 95, 1
Euclid Collaboration: Aussel, H., Tereno, I., Schirmer, M., et al. 2025, A&A, submitted
Euclid Collaboration: Bisigello, L., Massimo, M., Tortora, C., et al. 2024, A&A, 691, A1
Euclid Collaboration: Bisigello, L., Rodighiero, G., Fotopoulou, S., et al. 2025, A&A, submitted
Euclid Collaboration: Cropper, M., Al Bahlawan, A., Amiaux, J., et al. 2024, A&A, accepted, arXiv:2405.13492
Euclid Collaboration: Desprez, G., Paltani, S., Coupon, J., et al. 2020, A&A, 644, A31
Euclid Collaboration: Jahnke, K., Gillard, W., Schirmer, M., et al. 2024, A&A, accepted, arXiv:2405.13493
Euclid Collaboration: Lusso, E., Fotopoulou, S., Selwood, M., et al. 2024, A&A, 685, A108
Euclid Collaboration: Matamoro Zatarain, T., Fotopoulou, S., Ricci, F., et al. 2025, A&A, submitted
Euclid Collaboration: McCracken, H., Benson, K., et al. 2025, A&A, submitted
Euclid Collaboration: Mellier, Y., Abdurro'uf, Acevedo Barroso, J., et al. 2024, A&A, accepted, arXiv:2405.13491
Euclid Collaboration: Polenta, G., Frailis, M., Alavi, A., et al. 2025, A&A, submitted
Euclid Collaboration: Romelli, E., Kümmel, M., Dole, H., et al. 2025, A&A, submitted
Euclid Collaboration: Scaramella, R., Amiaux, J., Mellier, Y., et al. 2022, A&A, 662, A112
Euclid Collaboration: Selwood, M., Fotopoulou, S., Bremer, M. N., et al. 2025, A&A, 693, A250
Evans, I. N., Evans, J. D., Martínez-Galarza, J. R., et al. 2024, ApJS, 274, 22
Feltre, A., Charlot, S., & Gutkin, J. 2016, MNRAS, 456, 3354
Ferrarese, L. & Merritt, D. 2000, ApJ, 539, L9
Fotopoulou, S., Pacaud, F., Paltani, S., et al. 2016, A&A, 592, A5
Fotopoulou, S. & Paltani, S. 2018, A&A, 619, A14
Gebhardt, K., Bender, R., Bower, G., et al. 2000, ApJ, 539, L13
Georgakakis, A., Aird, J., Buchner, J., et al. 2015, MNRAS, 453, 1946
Georgakakis, A. & Nandra, K. 2011, MNRAS, 414, 992
Georgakakis, A., Rowan-Robinson, M., Babbedge, T. S. R., & Georgantopoulos, I. 2007, MNRAS, 377, 203
Green, K., Elmer, E., Maltby, D. T., et al. 2024, MNRAS, 531, 2551
Greene, J. E., Zakamska, N. L., Ho, L. C., & Barth, A. J. 2011, ApJ, 732, 9
Gültekin, K., Richstone, D. O., Gebhardt, K., et al. 2009, ApJ, 698, 198
Häring, N. & Rix, H.-W. 2004, ApJ, 604, L89
Harrison, C. M. & Ramos Almeida, C. 2024, Galaxies, 12, 17
Hasinger, G. 2008, A&A, 490, 905
Hasinger, G., Miyaji, T., & Schmidt, M. 2005, A&A, 441, 417
Heckman, T. M. & Best, P. N. 2014, A&A, 52, 589
Hickox, R. C. & Alexander, D. M. 2018, ARA&A, 56, 625
Hsu, L.-T., Salvato, M., Nandra, K., et al. 2014, ApJ, 796, 60
Husemann, B. & Harrison, C. M. 2018, Nature Astronomy, 2, 196–197
Ivezic, Z., Kahn, S. M., Tyson, J. A., et al. 2019, ApJ, 873, 111
Juneau, S., Bournaud, F., Charlot, S., et al. 2014, ApJ, 788, 88
Karsten, J., Wang, L., Margalef-Bentabol, B., et al. 2023, A&A, 675, A159
Kawamuro, T., Ueda, Y., Tazaki, F., & Terashima, Y. 2013, ApJ, 770, 157
Kirkpatrick, A., Pope, A., Charmandaris, V., et al. 2013, ApJ, 763, 123
Kluge, M., Comparat, J., Liu, A., et al. 2024, A&A, 688, A210
Kormendy, J. & Ho, L. C. 2013, ARA&A, 51, 511
Kyritsis, E., Zezas, A., Haberl, F., et al. 2025, A&A, 694, A128
Lang, D. 2014, ApJ, 147, 108
Laureijs, R., Amiaux, J., Arduini, S., et al. 2011, ESA/SRE(2011)12, arXiv:1110.3193
Lehmer, B. D., Xue, Y. Q., Brandt, W. N., et al. 2012, ApJ, 752, 46
Lundberg, S. & Lee, S.-I. 2017, arXiv e-prints, arXiv:1705.07874
Luo, B., Brandt, W. N., Xue, Y. Q., et al. 2017, ApJS, 228, 2
Lusso, E. & Risaliti, G. 2016, ApJ, 819, 154
Lynden-Bell, D. 1969, Nature, 223, 690
Lynden-Bell, D. & Pringle, J. E. 1974, MNRAS, 168, 603
Lyu, J., Alberts, S., Rieke, G. H., & Rujopakarn, W. 2022, ApJ, 941, 191
Maccacaro, T., Gioia, I. M., Wolter, A., Zamorani, G., & Stocke, J. T. 1988, ApJ, 326, 680
Maciaszek, T., Ealet, A., Gillard, W., et al. 2022, in SPIE, Vol. 12180, Space Telescopes and Instrumentation 2022: Optical, Infrared, and Millimeter Wave, ed. L. E. Coyle, S. Matsuura, & M. D. Perrin, arXiv:2210.10112
Madau, P. & Dickinson, M. 2014, ARA&A, 52, 415
Magorrian, J., Tremaine, S., Richstone, D., et al. 1998, AJ, 115, 2285
Mainzer, A., Bauer, J., Grav, T., et al. 2011, ApJ, 731, 53
Marchesi, S., Lanzuisi, G., Civano, F., et al. 2016, ApJ, 830, 100
Mechbal, S., Ackermann, M., & Kowalski, M. 2024, A&A, 685, A107
Meisner, A. M., Lang, D., & Schlegel, D. J. 2017, ApJ, 153, 38
Merloni, A., Bongiorno, A., Brusa, M., et al. 2014, MNRAS, 437, 3550
Merloni, A., Lamer, G., Liu, T., et al. 2024, A&A, 682, A34
Messias, H., Afonso, J. M., Salvato, M., Mobasher, B., & Hopkins, A. M. 2014, A&A, 562, A144
Morganti, R. 2017, Frontiers in Astronomy and Space Sciences, 4, 42
Nandra, K., Laird, E. S., Aird, J. A., et al. 2015, ApJS, 220, 10
Naylor, T., Broos, P. S., & Feigelson, E. D. 2013, ApJS, 209, 30
Oh, K., Koss, M., Markwardt, C. B., et al. 2018, ApJS, 235, 4
Oke, J. B. & Gunn, J. E. 1983, ApJ, 266, 713
Padovani, P., Alexander, D. M., Assef, R. J., et al. 2017, A&A Rev., 25, 2
Palanque-Delabrouille, N., Magneville, C., Yèche, C., et al. 2016, A&A, 587, A41
Park, T., Kashyap, V. L., Siemiginowska, A., et al. 2006, ApJ, 652, 610
Pedregosa, F., Varoquaux, G., Gramfort, A., et al. 2011, Journal of Machine Learning Research, 12, 2825
Peters, C. M., Richards, G. T., Myers, A. D., et al. 2015, ApJ, 811, 95
Peterson, B. M. 1997, An Introduction to Active Galactic Nuclei (Cambridge University Press)
Pierce, C. M., Lotz, J. M., Salim, S., et al. 2010, MNRAS, 408, 139
Pineau, F. X., Derriere, S., Motch, C., et al. 2017, A&A, 597, A89

Pović , M., Sánchez-Portal, M., García, A. M. P., et al. 2012, A&A, 541, A118
Predehl, P., Andritschke, R., Arefiev, V., et al. 2021, A&A, 647, A1
Pringle, J. E. & Rees, M. J. 1972, A&A, 21, 1
Pérez-Díaz, V. S., Martínez-Galarza, J. R., Caicedo, A., & D'Abrusco, R. 2024, MNRAS, 528, 4852
Richards, G. T., Fan, X., Newberg, H. J., et al. 2002, AJ, 123, 2945
Roster, W., Salvato, M., Krippendorf, S., et al. 2024, A&A, 692, A260
Rozemberczki, B., Watson, L., Bayer, P., et al. 2022, arXiv e-prints, arXiv:2202.05594
Salpeter, E. E. 1964, ApJ, 140, 796
Salvato, M., Buchner, J., Budavári, T., et al. 2018, MNRAS, 473, 4937
Salvato, M., Hasinger, G., Ilbert, O., et al. 2008, ApJ, 690, 1250
Salvato, M., Ilbert, O., Hasinger, G., et al. 2011, ApJ, 742, 61
Salvato, M., Ilbert, O., & Hoyle, B. 2019, Nature Astronomy, 3, 212
Salvato, M., Wolf, J., Dwelly, T., et al. 2022, A&A, 661, A3
Sani, E., Marconi, A., Hunt, L. K., & Risaliti, G. 2011, MNRAS, 413, 1479
Saxena, A., Salvato, M., Roster, W., et al. 2024, A&A, 690, A365
Shakura, N. I. & Sunyaev, R. A. 1973, A&A, 24, 337
Shankar, F., Bernardi, M., Sheth, R. K., et al. 2016, MNRAS, 460, 3119
Silva, D. R., Blum, R. D., Allen, L., et al. 2016, in AAS, Vol. 228, AAS Meeting Abstracts #228, 317.02
Smolčić, V., Novak, M., Delvecchio, I., et al. 2017, A&A, 602, A6
Stern, D., Assef, R. J., Benford, D. J., et al. 2012, ApJ, 753, 30
Suh, H., Civano, F., Trakhtenbrot, B., et al. 2020, ApJ, 889, 32
Sutherland, W. & Saunders, W. 1992, MNRAS, 259, 413
Temple, M. J., Hewett, P. C., & Banerji, M. 2021, MNRAS, 508, 737
Traulsen, I., Schwope, A. D., Lamer, G., et al. 2020, A&A, 641, A137
Urry, C. M. & Padovani, P. 1995, PASP, 107, 803
Vallenari, A., Brown, A. G. A., Prusti, T., et al. 2023, A&A, 674, A1
Veilleux, S. & Osterbrock, D. E. 1987, ApJS, 63, 295
Webb, N. A., Coriat, M., Traulsen, I., et al. 2020, A&A, 641, A136
Wright, E. L., Eisenhardt, P. R. M., Mainzer, A. K., et al. 2010, AJ, 140, 1868
Xue, Y. Q., Brandt, W. N., Luo, B., et al. 2011a, in ASP, Vol. 439, The Galactic Center: a Window to the Nuclear Environment of Disk Galaxies, ed. M. R. Morris, Q. D. Wang, & F. Yuan, 478
Xue, Y. Q., Luo, B., Brandt, W. N., et al. 2011b, ApJS, 195, 10
Zeraatgari, F. Z., Hafezianzadeh, F., Zhang, Y., et al. 2024, MNRAS, 527, 4677
Zou, H., Zhang, T., Zhou, Z., et al. 2017, ApJ, 153

[1] Max Planck Institute for Extraterrestrial Physics, Giessenbachstr. 1, 85748 Garching, Germany
[2] INAF-Osservatorio Astrofisico di Arcetri, Largo E. Fermi 5, 50125, Firenze, Italy
[3] Dipartimento di Fisica e Astronomia, Università di Firenze, via G. Sansone 1, 50019 Sesto Fiorentino, Firenze, Italy
[4] Department of Physics, Centre for Extragalactic Astronomy, Durham University, South Road, Durham, DH1 3LE, UK
[5] INAF-Osservatorio di Astrofisica e Scienza dello Spazio di Bologna, Via Piero Gobetti 93/3, 40129 Bologna, Italy
[6] Instituto de Astrofísica de Canarias (IAC); Departamento de Astrofísica, Universidad de La Laguna (ULL), 38200, La Laguna, Tenerife, Spain
[7] Institute of Space Sciences (ICE, CSIC), Campus UAB, Carrer de Can Magrans, s/n, 08193 Barcelona, Spain
[8] INAF-Osservatorio Astronomico di Capodimonte, Via Moiariello 16, 80131 Napoli, Italy
[9] School of Physics, HH Wills Physics Laboratory, University of Bristol, Tyndall Avenue, Bristol, BS8 1TL, UK
[10] Department of Mathematics and Physics, Roma Tre University, Via della Vasca Navale 84, 00146 Rome, Italy
[11] INAF-Osservatorio Astronomico di Roma, Via Frascati 33, 00078 Monteporzio Catone, Italy
[12] Instituto de Astrofísica de Canarias, Vía Láctea, 38205 La Laguna, Tenerife, Spain
[13] Universidad de La Laguna, Departamento de Astrofísica, 38206 La Laguna, Tenerife, Spain
[14] Dipartimento di Fisica e Astronomia "Augusto Righi" - Alma Mater Studiorum Università di Bologna, via Piero Gobetti 93/2, 40129 Bologna, Italy
[15] Université Paris-Saclay, CNRS, Institut d'astrophysique spatiale, 91405, Orsay, France
[16] ESAC/ESA, Camino Bajo del Castillo, s/n., Urb. Villafranca del Castillo, 28692 Villanueva de la Cañada, Madrid, Spain
[17] School of Mathematics and Physics, University of Surrey, Guildford, Surrey, GU2 7XH, UK
[18] INAF-Osservatorio Astronomico di Brera, Via Brera 28, 20122 Milano, Italy
[19] Université Paris-Saclay, Université Paris Cité, CEA, CNRS, AIM, 91191, Gif-sur-Yvette, France
[20] IFPU, Institute for Fundamental Physics of the Universe, via Beirut 2, 34151 Trieste, Italy
[21] INAF-Osservatorio Astronomico di Trieste, Via G. B. Tiepolo 11, 34143 Trieste, Italy
[22] INFN, Sezione di Trieste, Via Valerio 2, 34127 Trieste TS, Italy
[23] SISSA, International School for Advanced Studies, Via Bonomea 265, 34136 Trieste TS, Italy
[24] Dipartimento di Fisica e Astronomia, Università di Bologna, Via Gobetti 93/2, 40129 Bologna, Italy
[25] INFN-Sezione di Bologna, Viale Berti Pichat 6/2, 40127 Bologna, Italy
[26] INAF-Osservatorio Astronomico di Padova, Via dell'Osservatorio 5, 35122 Padova, Italy
[27] Space Science Data Center, Italian Space Agency, via del Politecnico snc, 00133 Roma, Italy
[28] Dipartimento di Fisica, Università di Genova, Via Dodecaneso 33, 16146, Genova, Italy
[29] INFN-Sezione di Genova, Via Dodecaneso 33, 16146, Genova, Italy
[30] Department of Physics "E. Pancini", University Federico II, Via Cinthia 6, 80126, Napoli, Italy
[31] Instituto de Astrofísica e Ciências do Espaço, Universidade do Porto, CAUP, Rua das Estrelas, PT4150-762 Porto, Portugal
[32] Faculdade de Ciências da Universidade do Porto, Rua do Campo de Alegre, 4150-007 Porto, Portugal
[33] Dipartimento di Fisica, Università degli Studi di Torino, Via P. Giuria 1, 10125 Torino, Italy
[34] INFN-Sezione di Torino, Via P. Giuria 1, 10125 Torino, Italy
[35] INAF-Osservatorio Astrofisico di Torino, Via Osservatorio 20, 10025 Pino Torinese (TO), Italy
[36] European Space Agency/ESTEC, Keplerlaan 1, 2201 AZ Noordwijk, The Netherlands
[37] Institute Lorentz, Leiden University, Niels Bohrweg 2, 2333 CA Leiden, The Netherlands
[38] Leiden Observatory, Leiden University, Einsteinweg 55, 2333 CC Leiden, The Netherlands
[39] INAF-IASF Milano, Via Alfonso Corti 12, 20133 Milano, Italy
[40] Centro de Investigaciones Energéticas, Medioambientales y Tecnológicas (CIEMAT), Avenida Complutense 40, 28040 Madrid, Spain
[41] Port d'Informació Científica, Campus UAB, C. Albareda s/n, 08193 Bellaterra (Barcelona), Spain
[42] Institute for Theoretical Particle Physics and Cosmology (TTK), RWTH Aachen University, 52056 Aachen, Germany
[43] INFN section of Naples, Via Cinthia 6, 80126, Napoli, Italy
[44] Institute for Astronomy, University of Hawaii, 2680 Woodlawn Drive, Honolulu, HI 96822, USA
[45] Dipartimento di Fisica e Astronomia "Augusto Righi" - Alma Mater Studiorum Università di Bologna, Viale Berti Pichat 6/2, 40127 Bologna, Italy
[46] Institute for Astronomy, University of Edinburgh, Royal Observatory, Blackford Hill, Edinburgh EH9 3HJ, UK
[47] Jodrell Bank Centre for Astrophysics, Department of Physics and Astronomy, University of Manchester, Oxford Road, Manchester M13 9PL, UK
[48] European Space Agency/ESRIN, Largo Galileo Galilei 1, 00044 Frascati, Roma, Italy
[49] Université Claude Bernard Lyon 1, CNRS/IN2P3, IP2I Lyon, UMR 5822, Villeurbanne, F-69100, France
[50] Institut de Ciències del Cosmos (ICCUB), Universitat de Barcelona (IEEC-UB), Martí i Franquès 1, 08028 Barcelona, Spain
[51] Institució Catalana de Recerca i Estudis Avançats (ICREA), Passeig de Lluís Companys 23, 08010 Barcelona, Spain

[52] UCB Lyon 1, CNRS/IN2P3, IUF, IP2I Lyon, 4 rue Enrico Fermi, 69622 Villeurbanne, France
[53] Mullard Space Science Laboratory, University College London, Holmbury St Mary, Dorking, Surrey RH5 6NT, UK
[54] Departamento de Física, Faculdade de Ciências, Universidade de Lisboa, Edifício C8, Campo Grande, PT1749-016 Lisboa, Portugal
[55] Instituto de Astrofísica e Ciências do Espaço, Faculdade de Ciências, Universidade de Lisboa, Campo Grande, 1749-016 Lisboa, Portugal
[56] Department of Astronomy, University of Geneva, ch. d'Ecogia 16, 1290 Versoix, Switzerland
[57] INAF-Istituto di Astrofisica e Planetologia Spaziali, via del Fosso del Cavaliere, 100, 00100 Roma, Italy
[58] INFN-Padova, Via Marzolo 8, 35131 Padova, Italy
[59] Aix-Marseille Université, CNRS/IN2P3, CPPM, Marseille, France
[60] Universitäts-Sternwarte München, Fakultät für Physik, Ludwig-Maximilians-Universität München, Scheinerstrasse 1, 81679 München, Germany
[61] INFN-Bologna, Via Irnerio 46, 40126 Bologna, Italy
[62] Institut d'Estudis Espacials de Catalunya (IEEC), Edifici RDIT, Campus UPC, 08860 Castelldefels, Barcelona, Spain
[63] NRC Herzberg, 5071 West Saanich Rd, Victoria, BC V9E 2E7, Canada
[64] Institute of Theoretical Astrophysics, University of Oslo, P.O. Box 1029 Blindern, 0315 Oslo, Norway
[65] Jet Propulsion Laboratory, California Institute of Technology, 4800 Oak Grove Drive, Pasadena, CA, 91109, USA
[66] Department of Physics, Lancaster University, Lancaster, LA1 4YB, UK
[67] Felix Hormuth Engineering, Goethestr. 17, 69181 Leimen, Germany
[68] Technical University of Denmark, Elektrovej 327, 2800 Kgs. Lyngby, Denmark
[69] Cosmic Dawn Center (DAWN), Denmark
[70] Institut d'Astrophysique de Paris, UMR 7095, CNRS, and Sorbonne Université, 98 bis boulevard Arago, 75014 Paris, France
[71] Max-Planck-Institut für Astronomie, Königstuhl 17, 69117 Heidelberg, Germany
[72] NASA Goddard Space Flight Center, Greenbelt, MD 20771, USA
[73] Department of Physics and Helsinki Institute of Physics, Gustaf Hällströmin katu 2, 00014 University of Helsinki, Finland
[74] Université de Genève, Département de Physique Théorique and Centre for Astroparticle Physics, 24 quai Ernest-Ansermet, CH-1211 Genève 4, Switzerland
[75] Department of Physics, P.O. Box 64, 00014 University of Helsinki, Finland
[76] Helsinki Institute of Physics, Gustaf Hällströmin katu 2, University of Helsinki, Helsinki, Finland
[77] Centre de Calcul de l'IN2P3/CNRS, 21 avenue Pierre de Coubertin 69627 Villeurbanne Cedex, France
[78] Laboratoire d'etude de l'Univers et des phenomenes eXtremes, Observatoire de Paris, Université PSL, Sorbonne Université, CNRS, 92190 Meudon, France
[79] Aix-Marseille Université, CNRS, CNES, LAM, Marseille, France
[80] SKA Observatory, Jodrell Bank, Lower Withington, Macclesfield, Cheshire SK11 9FT, UK
[81] Dipartimento di Fisica "Aldo Pontremoli", Università degli Studi di Milano, Via Celoria 16, 20133 Milano, Italy
[82] INFN-Sezione di Milano, Via Celoria 16, 20133 Milano, Italy
[83] University of Applied Sciences and Arts of Northwestern Switzerland, School of Computer Science, 5210 Windisch, Switzerland
[84] Universität Bonn, Argelander-Institut für Astronomie, Auf dem Hügel 71, 53121 Bonn, Germany
[85] INFN-Sezione di Roma, Piazzale Aldo Moro, 2 - c/o Dipartimento di Fisica, Edificio G. Marconi, 00185 Roma, Italy
[86] Department of Physics, Institute for Computational Cosmology, Durham University, South Road, Durham, DH1 3LE, UK
[87] Infrared Processing and Analysis Center, California Institute of Technology, Pasadena, CA 91125, USA
[88] Université Paris Cité, CNRS, Astroparticule et Cosmologie, 75013 Paris, France
[89] CNRS-UCB International Research Laboratory, Centre Pierre Binetruy, IRL2007, CPB-IN2P3, Berkeley, USA
[90] University of Applied Sciences and Arts of Northwestern Switzerland, School of Engineering, 5210 Windisch, Switzerland
[91] Institut d'Astrophysique de Paris, 98bis Boulevard Arago, 75014, Paris, France
[92] Institute of Physics, Laboratory of Astrophysics, Ecole Polytechnique Fédérale de Lausanne (EPFL), Observatoire de Sauverny, 1290 Versoix, Switzerland
[93] Aurora Technology for European Space Agency (ESA), Camino bajo del Castillo, s/n, Urbanizacion Villafranca del Castillo, Villanueva de la Cañada, 28692 Madrid, Spain
[94] Institut de Física d'Altes Energies (IFAE), The Barcelona Institute of Science and Technology, Campus UAB, 08193 Bellaterra (Barcelona), Spain
[95] School of Mathematics, Statistics and Physics, Newcastle University, Herschel Building, Newcastle-upon-Tyne, NE1 7RU, UK
[96] DARK, Niels Bohr Institute, University of Copenhagen, Jagtvej 155, 2200 Copenhagen, Denmark
[97] Waterloo Centre for Astrophysics, University of Waterloo, Waterloo, Ontario N2L 3G1, Canada
[98] Department of Physics and Astronomy, University of Waterloo, Waterloo, Ontario N2L 3G1, Canada
[99] Perimeter Institute for Theoretical Physics, Waterloo, Ontario N2L 2Y5, Canada
[100] Centre National d'Etudes Spatiales – Centre spatial de Toulouse, 18 avenue Edouard Belin, 31401 Toulouse Cedex 9, France
[101] Institute of Space Science, Str. Atomistilor, nr. 409 Măgurele, Ilfov, 077125, Romania
[102] Consejo Superior de Investigaciones Cientificas, Calle Serrano 117, 28006 Madrid, Spain
[103] Dipartimento di Fisica e Astronomia "G. Galilei", Università di Padova, Via Marzolo 8, 35131 Padova, Italy
[104] Institut für Theoretische Physik, University of Heidelberg, Philosophenweg 16, 69120 Heidelberg, Germany
[105] Institut de Recherche en Astrophysique et Planétologie (IRAP), Université de Toulouse, CNRS, UPS, CNES, 14 Av. Edouard Belin, 31400 Toulouse, France
[106] Université St Joseph; Faculty of Sciences, Beirut, Lebanon
[107] Departamento de Física, FCFM, Universidad de Chile, Blanco Encalada 2008, Santiago, Chile
[108] Universität Innsbruck, Institut für Astro- und Teilchenphysik, Technikerstr. 25/8, 6020 Innsbruck, Austria
[109] Satlantis, University Science Park, Sede Bld 48940, Leioa-Bilbao, Spain
[110] Instituto de Astrofísica e Ciências do Espaço, Faculdade de Ciências, Universidade de Lisboa, Tapada da Ajuda, 1349-018 Lisboa, Portugal
[111] Cosmic Dawn Center (DAWN)
[112] Niels Bohr Institute, University of Copenhagen, Jagtvej 128, 2200 Copenhagen, Denmark
[113] Universidad Politécnica de Cartagena, Departamento de Electrónica y Tecnología de Computadoras, Plaza del Hospital 1, 30202 Cartagena, Spain
[114] Kapteyn Astronomical Institute, University of Groningen, PO Box 800, 9700 AV Groningen, The Netherlands
[115] Dipartimento di Fisica e Scienze della Terra, Università degli Studi di Ferrara, Via Giuseppe Saragat 1, 44122 Ferrara, Italy
[116] Istituto Nazionale di Fisica Nucleare, Sezione di Ferrara, Via Giuseppe Saragat 1, 44122 Ferrara, Italy
[117] INAF, Istituto di Radioastronomia, Via Piero Gobetti 101, 40129 Bologna, Italy
[118] Université Côte d'Azur, Observatoire de la Côte d'Azur, CNRS, Laboratoire Lagrange, Bd de l'Observatoire, CS 34229, 06304 Nice cedex 4, France
[119] Department of Physics, Oxford University, Keble Road, Oxford OX1 3RH, UK

[120] Université PSL, Observatoire de Paris, Sorbonne Université, CNRS, LERMA, 75014, Paris, France
[121] Université Paris-Cité, 5 Rue Thomas Mann, 75013, Paris, France
[122] INAF - Osservatorio Astronomico di Brera, via Emilio Bianchi 46, 23807 Merate, Italy
[123] INAF-Osservatorio Astronomico di Brera, Via Brera 28, 20122 Milano, Italy, and INFN-Sezione di Genova, Via Dodecaneso 33, 16146, Genova, Italy
[124] ICL, Junia, Université Catholique de Lille, LITL, 59000 Lille, France
[125] ICSC - Centro Nazionale di Ricerca in High Performance Computing, Big Data e Quantum Computing, Via Magnanelli 2, Bologna, Italy
[126] Instituto de Física Teórica UAM-CSIC, Campus de Cantoblanco, 28049 Madrid, Spain
[127] CERCA/ISO, Department of Physics, Case Western Reserve University, 10900 Euclid Avenue, Cleveland, OH 44106, USA
[128] Technical University of Munich, TUM School of Natural Sciences, Physics Department, James-Franck-Str. 1, 85748 Garching, Germany
[129] Max-Planck-Institut für Astrophysik, Karl-Schwarzschild-Str. 1, 85748 Garching, Germany
[130] Laboratoire Univers et Théorie, Observatoire de Paris, Université PSL, Université Paris Cité, CNRS, 92190 Meudon, France
[131] Departamento de Física Fundamental. Universidad de Salamanca. Plaza de la Merced s/n. 37008 Salamanca, Spain
[132] Université de Strasbourg, CNRS, Observatoire astronomique de Strasbourg, UMR 7550, 67000 Strasbourg, France
[133] Center for Data-Driven Discovery, Kavli IPMU (WPI), UTIAS, The University of Tokyo, Kashiwa, Chiba 277-8583, Japan
[134] Ludwig-Maximilians-University, Schellingstrasse 4, 80799 Munich, Germany
[135] Max-Planck-Institut für Physik, Boltzmannstr. 8, 85748 Garching, Germany
[136] California Institute of Technology, 1200 E California Blvd, Pasadena, CA 91125, USA
[137] Department of Physics & Astronomy, University of California Irvine, Irvine CA 92697, USA
[138] Department of Mathematics and Physics E. De Giorgi, University of Salento, Via per Arnesano, CP-I93, 73100, Lecce, Italy
[139] INFN, Sezione di Lecce, Via per Arnesano, CP-193, 73100, Lecce, Italy
[140] INAF-Sezione di Lecce, c/o Dipartimento Matematica e Fisica, Via per Arnesano, 73100, Lecce, Italy
[141] Departamento Física Aplicada, Universidad Politécnica de Cartagena, Campus Muralla del Mar, 30202 Cartagena, Murcia, Spain
[142] Instituto de Física de Cantabria, Edificio Juan Jordá, Avenida de los Castros, 39005 Santander, Spain
[143] CEA Saclay, DFR/IRFU, Service d'Astrophysique, Bat. 709, 91191 Gif-sur-Yvette, France
[144] Institute of Cosmology and Gravitation, University of Portsmouth, Portsmouth PO1 3FX, UK
[145] Department of Computer Science, Aalto University, PO Box 15400, Espoo, FI-00 076, Finland
[146] Instituto de Astrofísica de Canarias, c/ Via Lactea s/n, La Laguna 38200, Spain. Departamento de Astrofísica de la Universidad de La Laguna, Avda. Francisco Sanchez, La Laguna, 38200, Spain
[147] Caltech/IPAC, 1200 E. California Blvd., Pasadena, CA 91125, USA
[148] Ruhr University Bochum, Faculty of Physics and Astronomy, Astronomical Institute (AIRUB), German Centre for Cosmological Lensing (GCCL), 44780 Bochum, Germany
[149] Department of Physics and Astronomy, Vesilinnantie 5, 20014 University of Turku, Finland
[150] Serco for European Space Agency (ESA), Camino bajo del Castillo, s/n, Urbanizacion Villafranca del Castillo, Villanueva de la Cañada, 28692 Madrid, Spain
[151] ARC Centre of Excellence for Dark Matter Particle Physics, Melbourne, Australia
[152] Centre for Astrophysics & Supercomputing, Swinburne University of Technology, Hawthorn, Victoria 3122, Australia
[153] Department of Physics and Astronomy, University of the Western Cape, Bellville, Cape Town, 7535, South Africa
[154] DAMTP, Centre for Mathematical Sciences, Wilberforce Road, Cambridge CB3 0WA, UK
[155] Kavli Institute for Cosmology Cambridge, Madingley Road, Cambridge, CB3 0HA, UK
[156] Department of Astrophysics, University of Zurich, Winterthurerstrasse 190, 8057 Zurich, Switzerland
[157] IRFU, CEA, Université Paris-Saclay 91191 Gif-sur-Yvette Cedex, France
[158] Oskar Klein Centre for Cosmoparticle Physics, Department of Physics, Stockholm University, Stockholm, SE-106 91, Sweden
[159] Astrophysics Group, Blackett Laboratory, Imperial College London, London SW7 2AZ, UK
[160] Univ. Grenoble Alpes, CNRS, Grenoble INP, LPSC-IN2P3, 53, Avenue des Martyrs, 38000, Grenoble, France
[161] Dipartimento di Fisica, Sapienza Università di Roma, Piazzale Aldo Moro 2, 00185 Roma, Italy
[162] Centro de Astrofísica da Universidade do Porto, Rua das Estrelas, 4150-762 Porto, Portugal
[163] HE Space for European Space Agency (ESA), Camino bajo del Castillo, s/n, Urbanizacion Villafranca del Castillo, Villanueva de la Cañada, 28692 Madrid, Spain
[164] Dipartimento di Fisica - Sezione di Astronomia, Università di Trieste, Via Tiepolo 11, 34131 Trieste, Italy
[165] Department of Astrophysical Sciences, Peyton Hall, Princeton University, Princeton, NJ 08544, USA
[166] Theoretical astrophysics, Department of Physics and Astronomy, Uppsala University, Box 515, 751 20 Uppsala, Sweden
[167] Mathematical Institute, University of Leiden, Einsteinweg 55, 2333 CA Leiden, The Netherlands
[168] School of Physics & Astronomy, University of Southampton, Highfield Campus, Southampton SO17 1BJ, UK
[169] Institute of Astronomy, University of Cambridge, Madingley Road, Cambridge CB3 0HA, UK
[170] Space physics and astronomy research unit, University of Oulu, Pentti Kaiteran katu 1, FI-90014 Oulu, Finland
[171] Center for Computational Astrophysics, Flatiron Institute, 162 5th Avenue, 10010, New York, NY, USA
[172] Department of Physics and Astronomy, University of British Columbia, Vancouver, BC V6T 1Z1, Canada

Appendix A: RF parameters

Understanding which features are most relevant to our model estimates is crucial for predictive accuracy. An ML model operating as a black box may produce predictions, but the lack of transparency raises questions about the reliability of the outcomes. This not only hinders immediate interpretability but also complicates post-analyses. The ML branch investigating the role each feature plays in the model's predictions is commonly referred to as 'feature importance'. To this end, we compute SHapley Additive exPlanations (SHAP; Lundberg & Lee 2017; Rozemberczki et al. 2022; Chen et al. 2022) values, based on a game-theoretic approach, by calculating the partial relevance for each feature. Based on a conditional expectation function, features are assigned importance values given their impact on test sample predictions. For a total achievable value v, SHAP values ϕ are computed via

$$\phi_f(v) = \frac{1}{p} \sum_S \frac{[v(S \cup \{f\}) - v(S)]}{\binom{p-1}{k(S)}} . \tag{A.1}$$

Given a given feature f, the summation is taken over all subsets S of the feature set $F = 1, 2, 3, \ldots, p$, which one can construct after excluding f. The size of S is given by $k(S)$ while $v(S)$ and $v(S \cup \{f\})$ refer to the value achieved by per subset before and after f joins S, respectively. This ensures that the contribution of each feature to a prediction collectively adds up to the value of the prediction as

$$\sum_{f=1}^{f=p} \phi_f(v) = v(F) . \tag{A.2}$$

However, achieving optimal accuracy in large modern data sets often involves complex models such as ensembles or deep-learning frameworks. Since it would be unfeasible to compute contributions across all possibilities of the feature space, we approximate SHAP values through Deep SHAP (Rozemberczki et al. 2022; Chen et al. 2022), which efficiently combines values computed for smaller network components into comprehensive values for the entire network, avoiding the need for heuristic choices in linearising components. The sign of SHAP values denotes whether a feature contributes to an increase or decrease in the predictive output, while the magnitude of the SHAP value quantifies the extent of the feature's influence on the prediction. Features with SHAP values close to zero for individual sources can be considered negligible or non-influential in this scenario. As a consequence, a feature can be seen as most influential if it exerts the most influence on the output across all predictions (Dey et al. 2022).

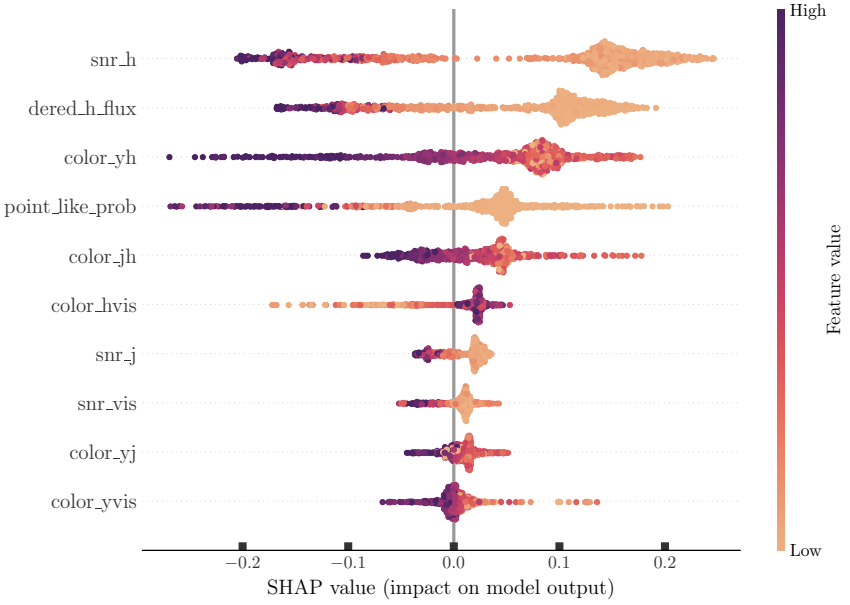

Fig. A.1. 'Beeswarm' plot showing the SHAP values for the features used in the RF model introduced in Sect. 4.1.2. Each point represents a SHAP value for a specific feature and data instance, illustrating the impact of that feature on the model's predictions. Features are sorted by their mean absolute SHAP values, with the most influential features appearing at the top. The colour gradient indicates the relative feature value (i.e., low to high), providing insight into how feature magnitude correlates with its effect on predictions.

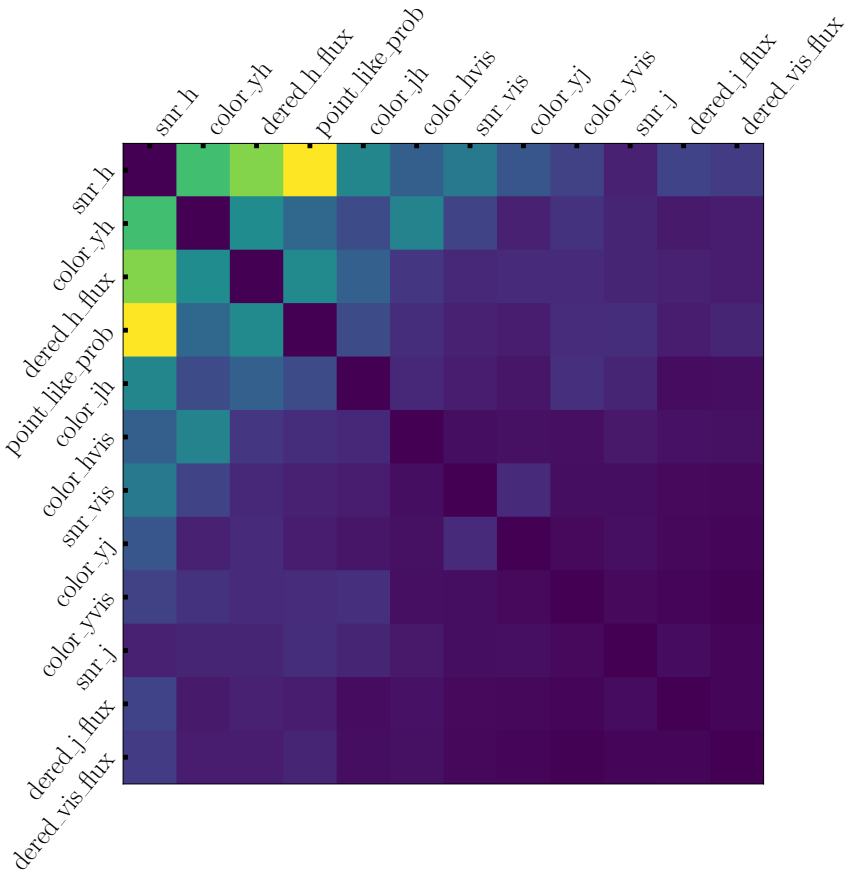

Fig. A.2. Correlation matrix displaying the pairwise Pearson correlation coefficients between the features used in the RF model introduced in Sect. 4.1.2. The colour intensity indicates the strength and direction of the correlations, with positive correlations shown in warm colours (yellow) and negative correlations in cool colours (blue). This visualisation helps identify interdependencies among features, which can inform feature selection and the interpretation of model performance.

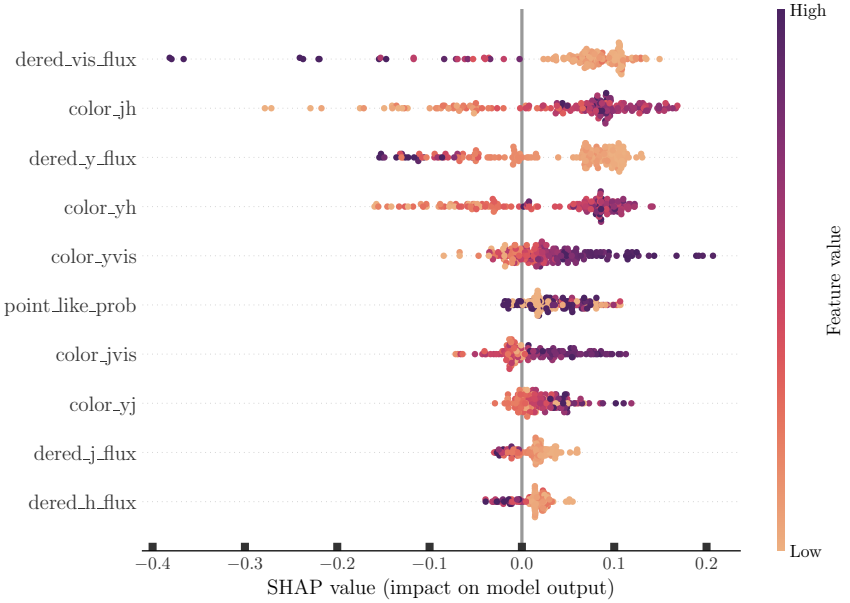

Fig. A.3. 'Beeswarm' plot showing the SHAP values for the features used in the RF model introduced in Sect. 5.2. Each point represents a SHAP value for a specific feature and data instance, illustrating the impact of that feature on the model's predictions. Features are sorted by their mean absolute SHAP values, with the most influential features appearing at the top. The colour gradient indicates the relative feature value (i.e., low to high), providing insight into how feature magnitude correlates with its effect on predictions.

Appendix B: Column description of released CTP catalogue

1. **Xray_ID**: X-ray source identifier (unique)
2. **Xray_RA**: J2000 Right Ascension of the X-ray source in the parent catalogue (deg)
3. **Xray_DEC**: J2000 Declination of the X-ray source in the parent catalogue (deg)
4. **Xray_CAT**: X-ray source catalogue
5. **Xray_pos_err**: Positional uncertainty of X-ray source (arcsec)
6. **Fx**: Mean 0.5 – 2 keV X-ray flux from all detections of the X-ray source (erg cm^{-2} s^{-1})
7. **EFx**: Error on the mean 0.5 – 2 keV X-ray flux from all detections of the X-ray source (erg cm^{-2} s^{-1})
8. **S_Nx**: Signal-to-noise ratio for Fx/EFx
9. **Fx_hard**: Mean hard (4XMM DR14: 2 – 4.5 keV, CSC 2.0: 2 – 7 keV and eROSITA DR1: 2–5 keV) X-ray flux from all detections of the X-ray source (erg cm^{-2} s^{-1})
10. **EUCLID_ID**: EUCLID source identifier (unique)
11. **EUCLID_RA**: J2000 Right Ascension of the counterpart in Q1 catalogue (deg)
12. **EUCLID_DEC**: J2000 Declination of the counterpart in Euclid catalogue (deg)
13. **EUCLID_pos_err**: Positional uncertainty of *Euclid* source (arcsec)
14. **Xray_EUCLID_ID**: Concatenation of X-ray_ID and EUCLID_ID (unique)
15. **EUCLID_Xray_proba**: Probability to be an X-ray emitter based on the RF
16. **Separation_EUCLID_Xray**: Distance between *Euclid* and X-ray source (arcsec)
17. **dist_bayesfactor**: Logarithm of ratio between prior and posterior, from separation, positional error, and number density (see Appendix in Salvato et al. 2018)
18. **dist_post**: Distance posterior probability comparing this association vs. no association (see Appendix in Salvato et al. 2018)
19. **bias_EUCLID_Xray_proba**: Probability weighting introduced by the *Euclid*-based prior (1 indicates no change)
20. **p_single**: Same as dist_post, but weighted by the prior (see Appendix in Salvato et al. 2018)
21. **p_any**: Probability that there is a counterpart in LS10 for each X-ray entry (see Appendix in Salvato et al. 2018)
22. **p_i**: Relative probability of the X-ray/*Euclid* match (see Appendix in Salvato et al. 2018)
23. **match_flag**: 1 for the most probable match; 2 for almost as good solutions (p_i/p_ibest > 0.5)
24. **EDF**: *Euclid* deep field
25. **LS10_FULLID**: Unique identifier of the LS10 source matched to the *Euclid* CTP (concatenation of RELEASE, BRICKID, and OBJID)
26. **LS10_RA**: J2000 Right Ascension of the LS10 source (deg)
27. **LS10_DEC**: J2000 Declination of the LS10 source (deg)
28. **Gal_proba**: Probability of being a Galactic rather than extragalactic source based on RF
29. **ra_spec**: J2000 Right Ascension of the spec-z match to the *Euclid* CTP (deg)
30. **dec_spec**: J2000 Declination of the spec-z match to the *Euclid* CTP (deg)
31. **z_spec**: Spectroscopic redshift
32. **z_err**: Error on the spectroscopic redshift
33. **Cat_spec**: Parent catalogue of the spec-z match
34. **phz**: `PICZL` photometric redshift (see Roster et al. 2024)
35. **phz_1sl**: Photo-z lower 1 sigma error
36. **phz_1su**: Photo-z upper 1 sigma error
37. **phz_3sl**: Photo-z lower 3 sigma error
38. **phz_3su**: Photo-z upper 3 sigma error
39. **z_final**: Spec-z when available; otherwise, photo-z
40. **Lx**: X-ray luminosity, assuming FlatLambdaCDM from `astropy.cosmology`